Transformation of Hm0 and Tm−1,0 over a model salt marsh

Dermentzoglou, Dimitrios; Tissier, Marion; Muller, Jos R.M.; Hofland, Bas; Lakerveld, Stijn; Borsje, Bas W.; Antonini, Alessandro

DOI
10.1016/j.coastaleng.2025.104900

Publication date
2025

Document Version
Final published version

Published in
Coastal Engineering

Citation (APA)
Dermentzoglou, D., Tissier, M., Muller, J. R. M., Hofland, B., Lakerveld, S., Borsje, B. W., & Antonini, A. (2025). Transformation of Hm0 and Tm−1,0 over a model salt marsh. *Coastal Engineering*, *204*, Article 104900. https://doi.org/10.1016/j.coastaleng.2025.104900

Coastal Engineering 204 (2026) 104900

Contents lists available at ScienceDirect

Coastal Engineering

journal homepage: www.elsevier.com/locate/coastaleng

Transformation of H_{m0} and $T_{m-1,0}$ over a model salt marsh

Dimitrios Dermentzoglou [a,*], Marion Tissier [a], Jos R.M. Muller [b], Bas Hofland [a], Stijn Lakerveld [a], Bas W. Borsje [b], Alessandro Antonini [a]

[a] Delft University of Technology, Department of Hydraulic Engineering, Stevinweg 1, Delft, 2628, The Netherlands
[b] University of Twente, Drienerlolaan 5, Enschede, 7522, The Netherlands

ARTICLE INFO

Dataset link: https://doi.org/10.4121/a2d39670-4a74-4a39-aebd-23956fafacbd.v1

Keywords:
Salt marsh
$T_{m-1,0}$
LiDAR
Wave flume
Dike
Attenuation
Scaled modeling

ABSTRACT

This research investigates how salt marshes contribute to both wave energy dissipation and spectral period transformation, advancing their role as a nature-based solution for coastal protection. Using laboratory simulations with a scaled barren foreshore, salt marsh and dike model, we examine the interactions between vegetation, water depth, and wave properties under varied conditions, including storm scenarios with irregular waves. Results indicate a case specific threshold at which the salt marsh model attenuates energy optimally, as for very shallow water depths wave energy is predominantly dissipated by the barren foreshore. The spectral wave period $T_{m-1,0}$ increases when waves propagate from deep to shallow water depths, as a result of wave breaking and generation of infragravity waves. The presence of salt marsh vegetation further enhances this effect by preferentially damping high frequency components. This highlights that an increase in $T_{m-1,0}$ in vegetated environments may not always correspond to an increased hydrodynamic load on the dike.

1. Introduction

In densely populated deltas around the globe, hard structures like dikes covered with a hard protection layer are commonly used as coastal protection measure. Such structures are static and will require heightening in the future as a result of sea level rise. Instead, grass covered dikes in combination with soft natural solutions like coastal wetlands could potentially be utilized, providing numerous benefits in terms of biodiversity, coastal protection and economy (van der Wal and Pye, 2004).

Salt marshes are a type of wetlands that can be found usually in the upper intertidal zone of moderate climates (Mcowen et al., 2017). They are climate-adaptive, as they can capture sediment and grow with rising sea level and attenuate wave energy from incoming storms (Vuik et al., 2016). Given that enough sediment is available, salt marshes can be resistant to climate change and sea level rise (*SLR*) (Kirwan and Megonigal, 2013; Best et al., 2018; Kirwan et al., 2010), while insufficient sediment supply leads to erosion (Mariotti and Fagherazzi, 2013). As a result, they could potentially reduce the need for future dike heightening investments. Moreover, grass dikes and salt marshes offer opportunities for nature development and recreational use and can store carbon very effectively, thereby providing environmental and societal benefits (Gedan et al., 2011). However, the large-scale implementation of salt marshes for coastal protection is constrained by the limited understanding of their behavior under extreme storm conditions. A fundamental consideration in this context is the determination of the dike crest height, which is typically based on the expected overtopping during such events (e.g., van Gent, 2002). Commonly used formulas for the calculation of these variables (e.g., EurOtop, 2018; Lashley et al., 2021; van Gent, 1999; Altomare et al., 2016) require prior knowledge of the spectral wave height (H_{m0}) and spectral wave period related to the first negative moment ($T_{m-1,0}$) at the toe of the dike. From this aspect, the implementation of salt marshes as an additional coastal defense requires a good understanding of the effect of a salt marsh on the variables above and, more generally, on hydrodynamics.

A key impact of vegetation in the nearshore zone is its significant role in mitigating wind-generated sea-swell waves. This process is influenced by multiple factors such as vegetation type (Willemsen et al., 2020), shoot stiffness (Bouma et al., 2013), the submergence ratio of plants (Yang et al., 2012), and the relative significant wave height (Möller, 2006), which all influence the ability of a salt marsh to dissipate wave energy. Although many experimental studies can be found on wave attenuation by vegetation (e.g., Augustin et al., 2009; Anderson and Smith, 2014; Maza et al., 2015; Zhang and Nepf, 2021; van Veelen et al., 2020; Zhao et al., 2023; Möller et al., 2014; Keimer et al., 2021), most of these focus on relatively low inundation depths ($d/l < 3.5$, where d is water depth, l is vegetation length) and the effect of vegetation during storm conditions with very high water levels is not

* Corresponding author.
E-mail address: d.dermentzoglou@tudelft.nl (D. Dermentzoglou).

https://doi.org/10.1016/j.coastaleng.2025.104900
Received 19 February 2025; Received in revised form 27 October 2025; Accepted 27 October 2025
Available online 30 October 2025

fully understood. Other natural salt marsh features, such as creeks and variations in bottom profile, could also play a role in wave attenuation, but their effect on near-dike wave characteristics is understudied.

The seaside boundary of a salt marsh can exhibit either a gradual incline, transitioning smoothly from the plant-covered surface to the barren foreshore, or it may feature a cliff (e.g. Muller et al., 2026; Brooks et al., 2021), which can range from a few centimeters to over a meter tall (Callaghan et al., 2010; Vuik et al., 2018). Commonly, it is an abrupt change in depth and can lead to wave reflection, which reduces the wave height of the incoming waves. However, under non-breaking wave conditions and if reflection is negligible, a decrease in depth can also increase the wave height. As a consequence, it is not clear how a more complex bathymetry influences the spectral wave height (H_{m_0}) and how it compares with the impact of the vegetation itself.

In addition to the wave attenuation properties, a salt marsh is expected to affect $T_{m-1,0}$. The development of long infra-gravity waves over a mildly sloping foreshore and the dissipation of shorter wind-generated waves due to wave breaking is expected to lead to an increasing dominance of long waves in shallow water (e.g., Bertin et al., 2018), leading to an increase in $T_{m-1,0}$ (Hofland et al., 2017). Altomare et al. (2016) also reports that $T_{m-1,0}$ increases over shallow foreshores and finds an overestimation of overtopping formulas (van Gent, 1999) for such conditions. As a step beyond integral dissipation models, Lowe et al. (2005) developed a framework to predict in-canopy velocity attenuation. Building on this concept, Jadhav et al. (2013) introduced a frequency-dependent drag coefficient using an in-canopy velocity reduction factor and a reorganized form of the energy dissipation model by Chen and Zhao (2012). These studies suggest that vegetation not only damps waves but also modifies the spectral shape, potentially altering $T_{m-1,0}$ as waves traverse the marsh. In engineering practice, spectral wave models like SWAN are commonly used to transform offshore wave conditions to near-dike locations, often accounting for the presence of vegetation. However, the default vegetation dissipation formulation in SWAN (Mendez and Losada, 2004; Suzuki et al., 2012) applies energy loss uniformly across the spectrum, neglecting the frequency-dependent nature of vegetation-induced attenuation. This simplification can lead to inaccuracies in the computed $T_{m-1,0}$, which is highly sensitive to the spectral energy distribution.

Several laboratory studies have been conducted in the past to investigate nearshore processes in the presence of salt marshes. Most of these studies focus solely on vegetation and its attenuating properties (e.g., Luhar and Nepf, 2016; Zhang et al., 2022; Contti Neto et al., 2025) while the effect of a salt marsh on $T_{m-1,0}$ has not been well studied. From this perspective, the main objective of this study is to quantify the impact of a schematized salt marsh on H_{m0} and $T_{m-1,0}$. This analysis relies on a unique set of small-scale laboratory experiments that include the schematization of a barren foreshore, a salt marsh and a dike. The experiment is designed to systematically investigate the effect of a complex bathymetry and vegetation for varying water levels, including high water levels (i.e. high d/l ratios) that have been seldom studied, despite their relevance for coastal protection (Möller et al., 2014). This will allow us to characterize the impact of the salt marsh on the key parameters used in overtopping formulas.

The study is structured as follows. Section 2 presents the lab set-up, the tested wave conditions, the scaling of the vegetation mimics (Section 2.1), the post processing (Section 2.2) and meta analysis of the data (Section 2.3). In Section 3 the results of the analysis are presented, further divided in Section 3.1 for H_{m0} evolution over a salt marsh, Section 3.2 for $T_{m-1,0}$. Section 4 discusses the implications of the findings and Section 5 presents the main conclusions.

2. Methodology

In this section we describe the employed methodology that is used to investigate the influence of the model salt marsh on wave dissipation and spectral wave characteristics. The section begins with a detailed description of the experimental setup, the wave conditions and instrumentation. We further elaborate the techniques used to replicate natural vegetation properties at laboratory scale. The post-processing procedures for data analysis are also discussed, including methods for decomposing water level signals and spectral analysis of wave energy.

Table 1
Experimental set-ups.

Setup	h_c [cm]	Vegetation
SU1	0	*X*
SU2	6	*X*
SU3	12	*X*
SU4	0	✓
SU5	6	✓
SU6	12	✓

2.1. Laboratory experiments

2.1.1. Experimental set-up

The laboratory experiments were conducted in the 42 m long, 0.8 m wide, 1 m high wave flume at the Hydraulic Engineering Laboratory of Delft University of Technology. This flume is equipped with a piston type wave-maker, able to generate regular and irregular waves. For these experiments, an idealized setup consisting of a barren foreshore, a salt marsh and a dike is installed in the flume (Fig. 1). The setup is a scaled model with a length scaling ratio of $N_L = 10$ (applied in both vertical and horizontal directions) of large scale experiments with a real salt marsh that were performed at a later stage in the Delta flume of Deltares (Antonini et al., 2024). These were designed to represent a typical barren foreshore-salt marsh-sea dike layout of the Southern Wadden Sea coast during extreme storm conditions. Setting a reference point at the wave generator ($x = 0$, Fig. 1), the wooden impermeable foreshore, placed at $x = 15.07$ m is made out of two parts; a steep slope part (1 : 9), 1.35 m long and a mild slope part (1 : 45), 4.05 m long. At the shoreward end of the foreshore, a smooth, wooden, horizontal, impermeable platform is installed to mimic a salt marsh. This is adjusted among three vertical positions above the foreshore, in order to create three different cliff heights of $h_c = 0, 6,$ *and* 12 cm (Fig. 1c). A dummy dike is installed at the end of the salt marsh, with a height of 1.15 m measured from the bottom of the flume and a slope of 1/3.6. The length of the salt marsh changes between 6.9, 7.1 and 7.3 m for the three different cases of h_c, as by raising the salt marsh platform an extra part of the dike needs to be covered. The experiments are also performed for the cases with and without vegetation on the salt marsh platform, leading to a total of 6 set-ups (Table 1). A summary of the instruments used is given in Table 2, also indicated in Fig. 1. In total, 5 collocated wave gauges (*WG 1-5*) and electromagnetic flow meters (*EMF 1-5*) are employed to measure water level and velocities respectively, at a sampling frequency $f_s = 200$ Hz. The vertical position of the *EMF* is set in the middle of the water column for each experiment. Additionally, two Sick LMS511 LiDAR sensors (*LS*1, *LS*2, Fig. 1) are utilized to measure water level fluctuations along the flume at $f_s = 10$ Hz. Since clean water does not effectively reflect LiDAR beams, a seeding agent, *Magspheres G25/60*, is added in the flume water at a concentration of 0.5 ml/l.

2.1.2. Test program

Two water depths over the salt marsh $d_m = 25$ and 40 cm are selected as representative cases (in scale) of typical and extreme inundation levels observed over salt marshes during storms (e.g., Vuik et al., 2016; Marin-Diaz et al., 2023). For $d_m = 25$ cm, three peak wave steepness values ($s_p = 3$–5%) are tested with $H_{m0} = 14$ cm, while for $d_m = 40$ cm we test four different target wave heights ($H_{m0} = 10$–16 cm) with $s_p = 4\%$. These seven experiments are tested across all three cliff configurations with $h_c = 0$ cm (IR03–IR05, IR12–IR15), $h_c = 6$ cm

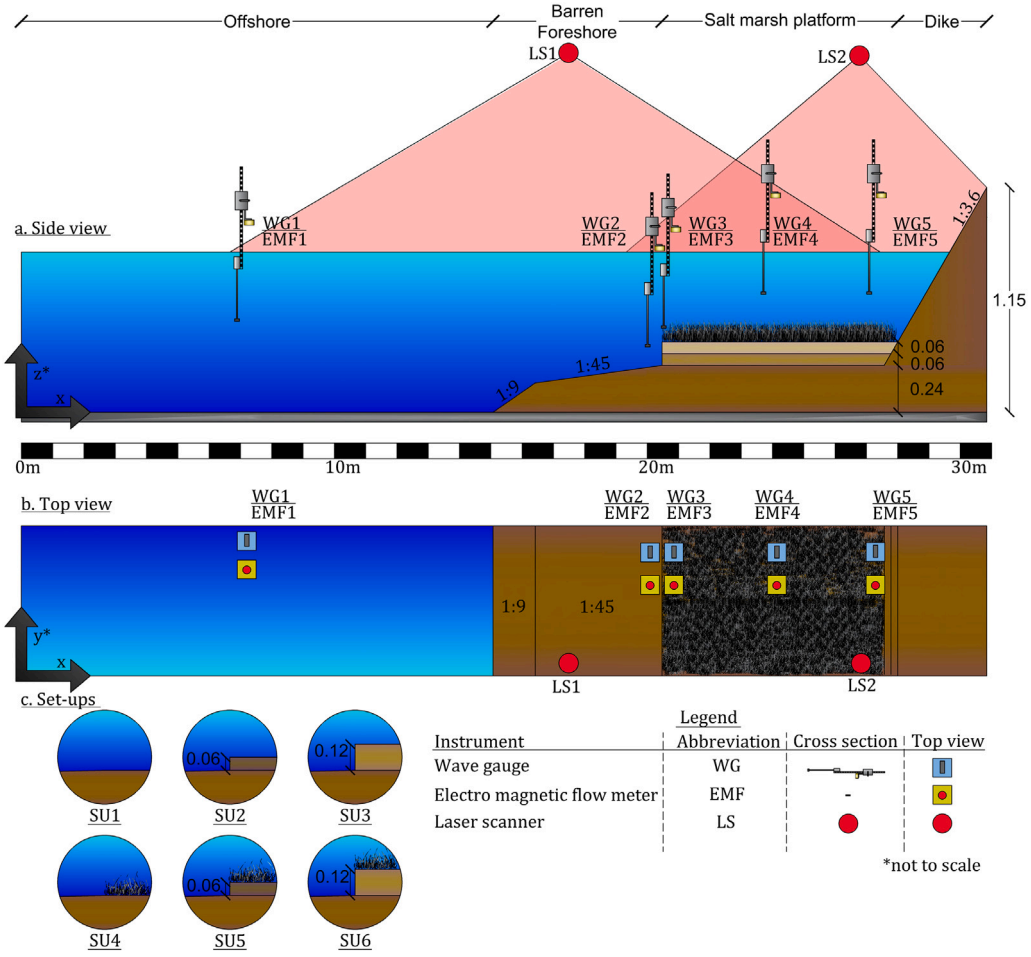

Fig. 1. a: Side view of experimental set-up. b: Top view. c: Zoomed side view around the salt marsh edge, distinguishing the set-ups (Table 1).

Table 2
List of used instruments, comprising 5 collocated WG and EMF and 2 $LS.WG5$ and $EMF5$ position depends on the set-up and are always set at the toe.

Instrument	x [m]	Sampling frequency [Hz]
WG1	7.15	200
WG2	20.36	200
WG3	20.68	200
WG4	23.96	200
WG5	27.34, 27.56, 27.78	200
EMF1	7.15	200
EMF2	20.36	200
EMF3	20.68	200
EMF4	23.96	200
EMF5	27.34, 27.56, 27.78	200
LS1	17.50	10
LS2	26.65	10

(IR24–IR30) and $h_c = 12$ cm (IR31–IR37). To enable direct comparisons between cases with and without a cliff, additional experiments are considered for $h_c = 0$ cm (IR06–IR11 and IR16–IR23) with matching offshore conditions to the cases of $h_c = 6$ and 12 cm. Two more low water depth cases (IR01 and IR02) are also included for the case without a cliff to increase coverage of the tested submergence ratio of vegetation (d_m/l, where l is the length of vegetation shoots). The selected wave steepness range ($s_p = 3$–5%) reflects typical values of deep-water wind-generated waves (e.g., Myrhaug, 2018). Wave heights are chosen so as to span a relevant range, to allow comparisons of identical wave heights at different water depths and to ensure that $d_m/L_p > 0.05$, avoiding strong depth-limited breaking over the salt marsh (where $L_p = H_{m0}/s_p$).

The above considerations lead to a total 37 wave conditions, each generated using JONSWAP spectra with a peak enhancement factor of 3.3. These were performed with a barren bottom (SU1, SU2, SU3, corresponding to $h_c = 0, 6, 12$ cm) and with vegetation (SU4, SU5, SU6) resulting in 74 experiments with a submergence ratio of plants $d_m/l = 1.8$–5.8 (Table 3). The duration of each experiment is planned for $1000T_p$, (1200 waves) where T_p is the peak spectral period calculated using L_p and the dispersion relationship.

2.1.3. Vegetation scaling

A scaled-down meadow is installed during the experiments to simulate a vegetated salt marsh. The overall adopted canopy scaling process envisages two main steps: the scaling and the clustering of shoots. In this subsection, we use the indices 0, 1 and 2 to describe the vegetation variables for the target vegetation in prototype scale, the scaled canopy resulting from the first transformation step and the clustered vegetation resulting from the second transformation step respectively.

Leaves of salt marsh species can contribute between 40–80% of the total drag force (Jalonen and Järvelä, 2013; Zhang and Nepf, 2021). However, the cylindrical model is employed as it is better suited to simulate wave attenuation under storm conditions, which primarily occur during winter when salt marsh vegetation has shed its leaves. As a result, the model consists of cylindrical neoprene shoots with a diameter $D_2 = 2$ mm, $l_2 = 9$ cm long, a material density $\rho_2 = 1230$ kg/m^3 and a canopy density $S_2 = 8100$ shoots/m^2. A 3-point bending test is performed with an Instron EMSYSL7049 flexure test machine on a hundred samples, measuring the mean value of Young's

Table 3
Target experimental wave states with the corresponding target offshore water depth (d_o), water depth above the salt marsh (d_m), submergence ratio of salt marsh vegetation (d_m/l), spectral wave height (H_{m0}), peak spectral wave period (T_p) peak wave steepness (s_p), cliff height (h_c) and tested set-ups.

No	d_o [cm]	d_m [cm]	d_m/l [−]	H_{m0} [cm]	T_p [s]	s_p [−]	h_c [cm]	Set-up
IR01	40	16	1.8	12	1.68	4	0	SU1-SU4
IR02	46	22	2.4	12	1.61	4	0	SU1-SU4
IR03	49	25	2.8	14	1.78	4	0	SU1-SU4
IR04	49	25	2.8	14	2.27	3	0	SU1-SU4
IR05	49	25	2.8	14	1.50	5	0	SU1-SU4
IR06	55	31	3.4	14	1.72	4	0	SU1-SU4
IR07	55	31	3.4	14	2.18	3	0	SU1-SU4
IR08	55	31	3.4	14	1.46	5	0	SU1-SU4
IR09	61	37	4.1	14	1.68	4	0	SU1-SU4
IR10	61	37	4.1	14	2.10	3	0	SU1-SU4
IR11	61	37	4.1	14	1.43	5	0	SU1-SU4
IR12	64	40	4.4	10	1.32	4	0	SU1-SU4
IR13	64	40	4.4	12	1.48	4	0	SU1-SU4
IR14	64	40	4.4	14	1.66	4	0	SU1-SU4
IR15	64	40	4.4	16	1.83	4	0	SU1-SU4
IR16	70	46	5.1	10	1.30	4	0	SU1-SU4
IR17	70	46	5.1	12	1.46	4	0	SU1-SU4
IR18	70	46	5.1	14	1.62	4	0	SU1-SU4
IR19	70	46	5.1	16	1.79	4	0	SU1-SU4
IR20	76	52	5.8	10	1.29	4	0	SU1-SU4
IR21	76	52	5.8	12	1.44	4	0	SU1-SU4
IR22	76	52	5.8	14	1.60	4	0	SU1-SU4
IR23	76	52	5.8	16	1.76	4	0	SU1-SU4
IR24	55	25	2.8	14	1.72	4	6	SU2-SU5
IR25	55	25	2.8	14	2.18	3	6	SU2-SU5
IR26	55	25	2.8	14	1.46	5	6	SU2-SU5
IR27	70	40	4.4	10	1.30	4	6	SU2-SU5
IR28	70	40	4.4	12	1.46	4	6	SU2-SU5
IR29	70	40	4.4	14	1.62	4	6	SU2-SU5
IR30	70	40	4.4	16	1.79	4	6	SU2-SU5
IR31	61	25	2.8	14	1.68	4	12	SU3-SU6
IR32	61	25	2.8	14	2.10	3	12	SU3-SU6
IR33	61	25	2.8	14	1.43	5	12	SU3-SU6
IR34	76	40	4.4	10	1.29	4	12	SU3-SU6
IR35	76	40	4.4	12	1.44	4	12	SU3-SU6
IR36	76	40	4.4	14	1.60	4	12	SU3-SU6
IR37	76	40	4.4	16	1.76	4	12	SU3-SU6

Modulus at $E_{y,2} = 8$ MPa. These dimensions and mechanical properties of the material were selected to mimic typical field values identified for *Spartina alteniflora* (Zhang et al., 2022) such as $S_0 = 191$ shoots/m^2, $D_0 = 8.5$ mm, $\rho_0 = 840$ kg/m^3 and stem elasticity $E_{y,0} = 1$ GPa.

For the first transformation step, the plant properties are scaled according to Zhang and Nepf (2021), which utilizes a scaling law for the dynamic reconfiguration of plants. In this model, plant orientation relies on three dimensionless parameters: the Buoyancy number (Bu), the Cauchy number (Ca), and the plant length ratio (L_b) (Eq. (1)). Ca is used to scale the elasticity of the shoots, Bu to scale the material density and L_b is used to scale the length of the plant relative to the prototype.

$$Ca = \frac{\rho_w A u^2}{EI/l^2},\ Bu = \frac{\Delta\rho g V}{EI/l^2},\ L_b = \frac{l}{A_w} = \frac{l\omega}{u} \tag{1}$$

In these equations $\Delta\rho = \rho_w - \rho$ is the material density difference between vegetation (ρ) and water (ρ_w), $g = 9.81$ m/s^2 is the gravity constant, D and l are the plant diameter and length, A and V are the frontal area and volume of the individual plant element, I is the momentum of inertia, A_w is the wave excursion, ω_p the peak angular frequency, u is the characteristic velocity on top of the vegetation field. To define the latter for the case of an irregular wave field, we use the target wave properties of experiment $IR15$ (Table 3) and calculate a 5th order Stokes solution (Zhao and Liu, 2022) right on top of the vegetation field, as shown in Table 4. The velocity and wave characteristics on prototype scale are obtained by applying a *Froude* scaling on the small scale wave characteristics, while the number of shoots/m^2 after the first transformation is calculated as $S_1 = S_0 N_L^2$. Through the first scaling step the flexibility is preserved by keeping Ca and L_b in the same order of magnitude. On the contrary, it results in plants with a small diameter ($D = 8.5$ mm/$N_L = 0.85$ mm) and lower velocities in comparison to the prototype, leading to a very small Reynolds vegetation number (Table 4, Scaling), defined as $Re_v = \frac{uD}{\nu}$, where u is a characteristic velocity on the individual plant element and ν is the kinematic viscosity. Applying a kinematic similarity, we calculate that in the field we expect values that are $Re_{v,0}/Re_{v,1} = (u_0 D_0/\nu)/(u_1 D_1/\nu) = N_L^{1.5} \approx 31.6$ times larger, which could potentially induce scaling effects in the model, since damping significantly increases for very low Reynolds numbers (Anderson and Smith, 2014).

Table 4
Two-step vegetation scaling. For the calculation of the dimensionless parameters, the target wave properties of experiment $IR15$ are used to calculate the characteristic velocity on the top part of the plant ($H_s = 0.16$ cm, $s = 4\%$, $u = 0.44$ m/s). The dimensionless numbers at the Clustering column are calculated using the properties of the selected material ($\rho_2 = 1230$ kg/m^3 and $E_{y,2} = 0.008$ GPa).

Variable	Symbol	Units	Prototype (0)	Scaling (1)	Clustering (2)
Canopy density	S	1/m^2	191	19 100	8118
Diameter	D	mm	8.5	0.85	2
Length	l	cm	90	9	9
Elasticity	E_y	GPa	1	0.1	0.008
Material density	ρ	kg/m^3	840	840	1230
Water density	ρ_w	kg/m^3	1010	1000	1000
Velocity	u	m/s	1.40	0.44	0.44
Wave height	H_{m0}	m	1.6	0.16	0.16
Wave steepness	s_p	–	4	4	4
Cauchy	Ca	–	48	47	45
Blade length ratio	L_b	–	0.7	0.7	0.7
Reynolds	Re	–	11 900	376	885
Buoyancy	Bu	–	1.1	1.0	−3.3

In order to mitigate this scaling effect, a second transformation is applied by clustering multiple shoots into one, increasing Re_v. By using $D_2 = 2$ mm, we do this on the basis of preserving the total drag force on the meadow as:

$$S_1 F_{D,1} = S_2 F_{D,2} \rightarrow S_2 = S_1 \frac{\frac{1}{2}\rho C_D A_1 u^2}{\frac{1}{2}\rho C_D A_2 u^2} = S_1 \frac{D_1}{D_2} \tag{2}$$

where $F_D = \frac{1}{2}\rho C_D A u^2$ is the drag force on individual shoots, C_D is a drag coefficient, $A = Dl$ is the frontal area of the plant. Applying a kinematic similarity for the scaling of velocity and using the values of D_0 and D_2, we calculate that $Re_{v,0}/Re_{v,2} \approx 13.4$ and the Reynolds scaling effect is reduced by a factor of $31.6/13.4 \approx 2.4$. At the same time, the value of $E_{y,2}$ is calculated in order to preserve Ca in the same order of magnitude after clustering and increasing D, preserving the flexibility. The plant material density is comparable to the density of water so plant buoyancy does not impact the blade posture significantly and Bu can be neglected (Zhang and Nepf, 2021). The two step scaling down process is summarized in Fig. 2, while a view of the constructed meadow is shown in Fig. 3.

2.2. Post-processing

Post-processing procedures are applied to the data collected from LS, WG and EMF. The signal retrieved from the LS is initially in the form of spherical coordinates. To process this data, the position of each scanner is first accurately determined. Subsequently, transformations are applied to convert the raw spherical coordinate dataset into a Cartesian coordinate system, as outlined by Oosterlo et al. (2021). The spatial resolution of the resulting dataset over the x axis varies spatially and is coarser at the edges of the scanning area with an average 4 cm, a minimum 2 cm and a maximum 10.5 cm among all

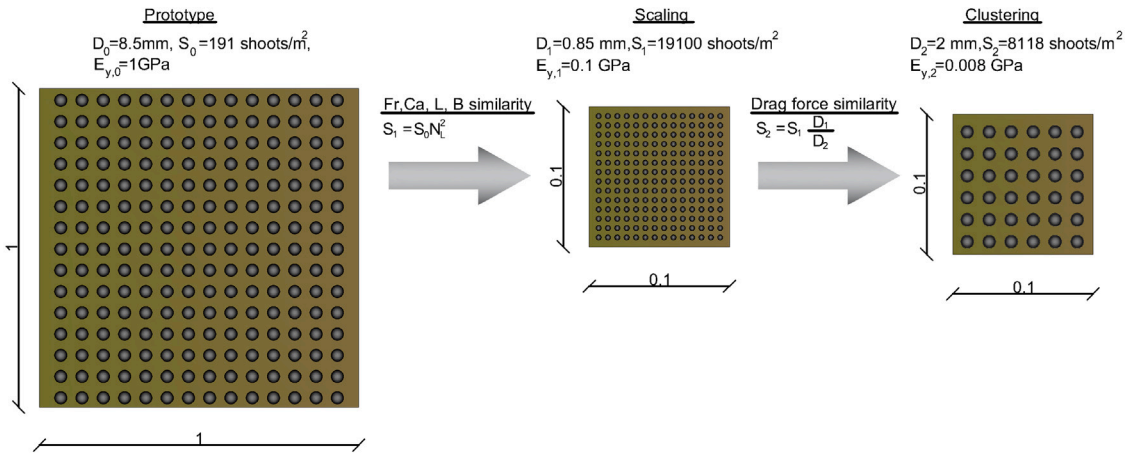

Fig. 2. Visualization of the two step scaling.

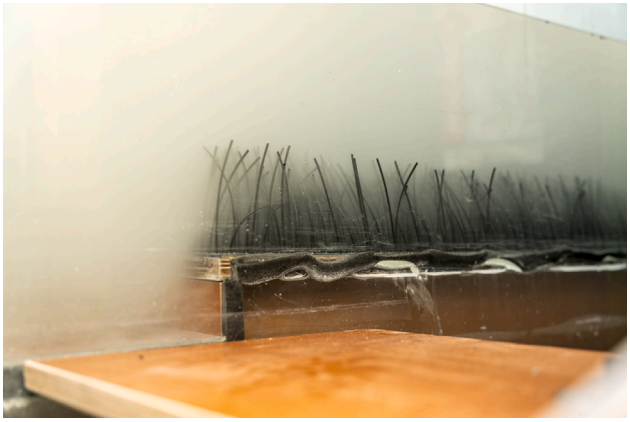

Fig. 3. Side view of the constructed meadow and the cliff.

experiments. This dataset is then linearly interpolated in space and in time to create a dense array of water level signals with a temporal resolution $\Delta t = 0.1$ s and a spatial resolution $\Delta x = 0.1$ m for each LS. A *Hampel* filter (e.g., Pearson et al., 2016) with a window width 1 s is applied to remove outliers and the resulting gaps in the dataset are filled using linear interpolation. As the resulting signals from the two LS have an overlapping area of about 5 m, a linear weighting function is used to combine the two signals into one (Fig. 4a, η_{LS}).

The LS operates on a different system than the WG and EMF, so its signal is aligned using cross-correlation. The processed LS signal is interpolated at the location of $WG4$ and cross-correlation is applied to compute the similarity between the interpolated LS signals and $WG4$ signal as a function of their relative time shift. The time lag corresponding to the maximum cross-correlation is used to align the LS signals with the WG and EMF signals. To ensure the analysis focuses on the stationary phase of the experiments, data from the beginning of the recordings up to $100T_p$ s after the wave generator starts are removed from all datasets.

2.3. Data analysis

η_{LS} is decomposed into an incident ($\eta_{i,R}$) and reflected ($\eta_{r,R}$) water level signal at each spatial grid point using the Radon transform (Almar et al., 2016). To do this, the standard grid ($\Delta x = 0.1$ m, $\Delta t = 0.1$ s) is reinterpolated into a finer mesh of $\Delta t = 0.016$ s and $\Delta x = 0.01$ m, as finer ratios of $t/\Delta t$ and $x/\Delta x$ reduce the errors of the method. The resulting incident and reflected wave components are reinterpolated back to the standard $\Delta x = 0.1$ s, $\Delta t = 0.1$ s grid. The signals from the collocated WG and EMF are also decomposed using a collocated decomposition method (Buckley et al., 2015) to extract incident ($\eta_{i,B}$) and reflected ($\eta_{r,B}$) wave components. Following this, we perform a spectral analysis on the retrieved incident signals ($\eta_{i,R}, \eta_{i,B}$), by dividing the detrended time series into blocks of $10T_p$, calculating the variance density spectra and averaging the spectra over the blocks to obtain the spectral density per frequency $P(f)$.

Fig. 5 presents the spectra retrieved from $\eta_{i,B}$ at the toe of the dike ($WG5 - EMF5$). In this figure, the spectral density (P) for each experiment is normalized by its maximum value, and the frequency axis is made dimensionless using the offshore peak frequency f_p. This normalization is applied to emphasize the spectral shape rather than absolute energy content, as the shape governs the spectral wave period $T_{m-1,0}$. It can be seen that secondary peaks develop as a result of non-linear wave–wave interactions, leading to energy transfers towards lower and higher frequencies. To quantify the frequency distribution of the energy, the spectra are further separated into a low ($f/f_p < 0.5$) frequency band, used to characterize the infragravity wave energy, and a main ($f/f_p > 0.5$) frequency band that contains the peak and its superharmonics.

H_{m0} and $T_{m-1,0}$ are then calculated for the low, main and entire frequency bands as $H_{m0} = 4\sqrt{m_0}$ and $T_{m-1,0} = m_{-1}/m_0$, where $m_n = \int_{f_1}^{f_2} P_{(f)} f^n df$, f_1 and f_2 are the bounds of the considered frequency band. Further in the manuscript, the superscripts *low*, *main* and *tot* are used to distinguish between variables that have been calculated using the low, main or entire frequency band.

Fig. 6 compares H_{m0}^{tot} and $T_{m-1,0}^{tot}$ calculated using $\eta_{i,R}$ to the values obtained from $\eta_{i,B}$ for all experiments. The results reveal a satisfactory agreement between the two methods for calculating H_{m0}, with a coefficient of determination $R^2 \approx 0.99$. However, a significant disparity arises in the calculation of $T_{m-1,0}$ ($R^2 \approx 0.83$). Unlike H_{m0}, which is only influenced by the total energy contained in a spectrum, $T_{m-1,0}$ is influenced by the distribution of energy across the frequency bands. LS measurements, while effective, are less accurate than WG measurements with the largest errors found in the low frequency band. Furthermore, in the cases with large deviations observed in Fig. 6, the Radon transform altered the total spectral distribution, impacting the reliability of $T_{m-1,0}$ calculations. As a result, in Section 3, we use the incoming wave signals processed via the Radon transform to study the evolution of wave height over the salt marsh. Conversely, we use the incoming wave signals produced using the collocated decomposition to analyze $T_{m-1,0}$, ensuring accuracy and consistency in the interpretation of the spectral wave period. Therefore the wave height is available with a much higher spatial resolution than the spectral period.

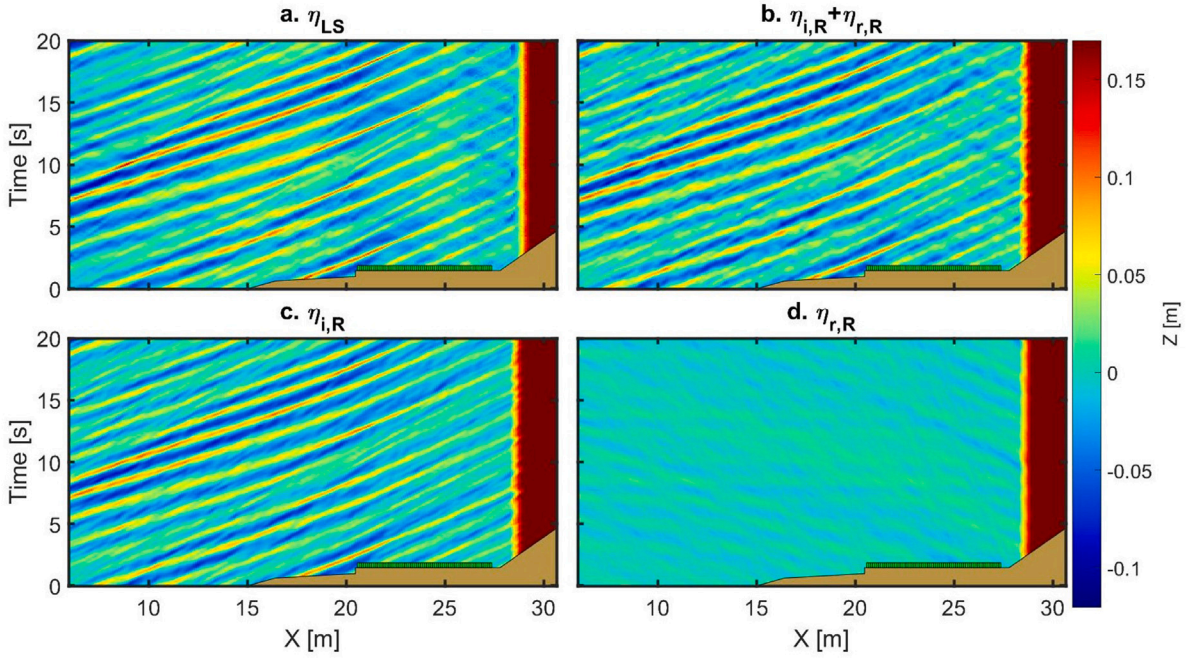

Fig. 4. Example of space–time diagram of: a: the raw surface elevation (η_{LS}) measured from the still water surface, b: Incident water level plus reflected water level after the Radon transform ($\eta_i + \eta_r$) c: Incident water level (η_i) d: reflected water level (η_r).

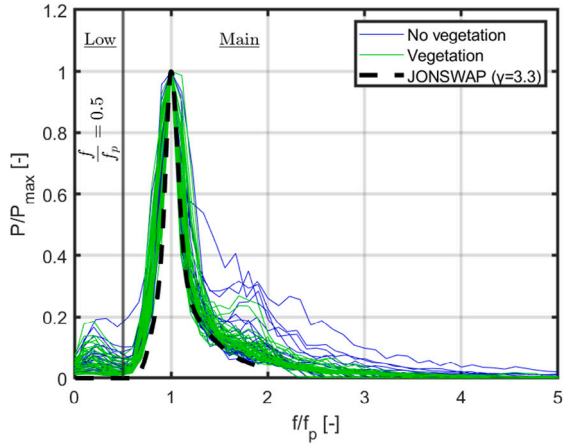

Fig. 5. Dimensionless spectra from all experiments at the toe of the dike without vegetation (blue), with vegetation (green) calculated using $\eta_{i,B}$, along with the defined frequency bands used for wave statistics. The black solid line is the theoretical JONSWAP spectrum with a peak enhancement factor $\gamma = 3.3$.

3. Results

In this section, the evolution of spectral wave height H_{m0} (Section 3.1) and $T_{m-1,0}$ (Section 3.2) are examined.

3.1. Wave height

Fig. 7 illustrates the evolution of H_{m0} along the flume for the different frequency bands (Section 2), under varying conditions (d_m = 0.16 m, 0.22 m and 0.40 m, where d_m is the water depth above the salt marsh), for the case without a cliff, with and without vegetation. Energy from the main frequency band is dissipated for all cases, while the low frequency band either grows slightly for the cases without vegetation or dissipates at a much lower rate compared to the main frequency band. Despite this, the main frequency band still dominates over the entire profile, with low frequency waves representing at most 5.6% of the total wave energy at the edge of the salt marsh and 1.8% on average among all experiments. At shallow water depths ($d_m = 0.16$ m), waves initially shoal as they propagate over the barren foreshore ($X \approx 16$ m), then begin breaking ($X \approx 17$ m), resulting in a reduction of wave height. Vegetation contributes to dissipation under these conditions, yet its relative contribution becomes more pronounced for higher water depths. For moderate water depth (0.22 m), vegetation dissipates more energy as less energy is dissipated by breaking over the foreshore. At higher water depths (0.40 m), both wave breaking and dissipation by vegetation diminish.

As a result, a spatial description of wave dissipation is crucial to separate the amount of energy dissipated by wave breaking and vegetation.

In the following, we investigate the cross-shore evolution of the energy in the main frequency band as it dominates over the profile. Assuming that the energy loss by bottom friction is negligible and that nonlinear energy transfers towards the low frequency band are small, the time-averaged energy balance is given by (Mendez and Losada, 2004):

$$\frac{\partial E c_g}{\partial x} = -\langle e_b \rangle - \langle e_v \rangle \tag{3}$$

where $\langle e_b \rangle$ and $\langle e_v \rangle$ are the dissipation induced by wave breaking and vegetation in the main frequency band, $E = \frac{1}{8}\rho g \left(H_{rms}^{main}\right)^2$, with $H_{rms}^{main} = H_{m0}^{main}/\sqrt{2}$, is the energy in this frequency band and c_g is the group velocity calculated from linear wave theory using the offshore T_p. The average energy dissipation rate per unit area caused by wave breaking is:

$$\langle e_b \rangle = \frac{3\sqrt{\pi}}{16}\rho g \frac{B^3 f_p}{\gamma_b^4 d^5}\left(H_{rms}^{main}\right)^7 \tag{4}$$

where γ_b is an adjustable parameter (Miche, 1944). B was introduced by Thornton and Guza (1983) and represents the percentage of foam on the face of the wave and the intensity of wave breaking. For the sake of simplicity, we assume $B = 1$ for the following analyses.

The average energy dissipation rate per unit area due to vegetation in the main frequency band is expressed as (Mendez and Losada, 2004):

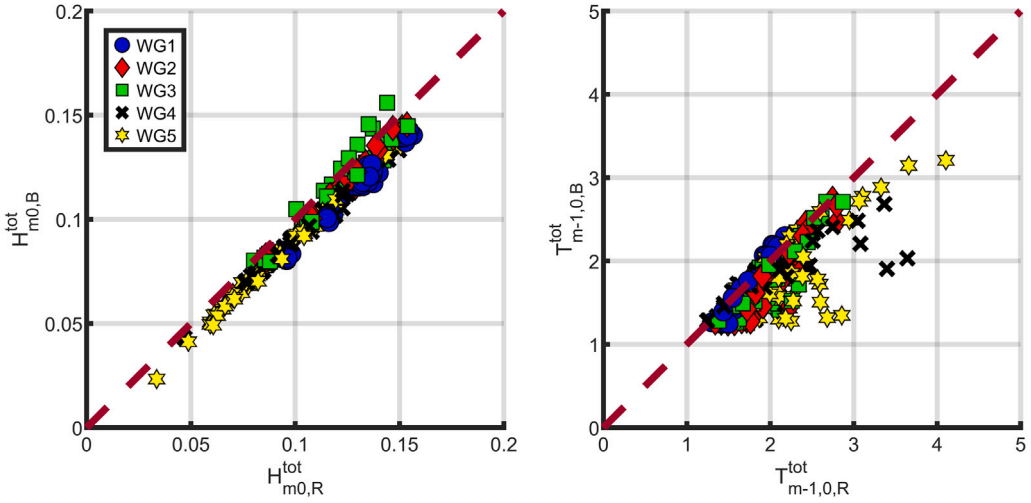

Fig. 6. Left: Comparison of H^{tot}_{m0} calculated from the incident water level that is derived through the processed LS signal and the Radon transformation ($\eta_{i,R}$) versus the one from the $WG-EMF$ and the collocated decomposition ($\eta_{i,B}$), for all experiments. Right: Similar comparison for $T^{tot}_{m-1,0}$.

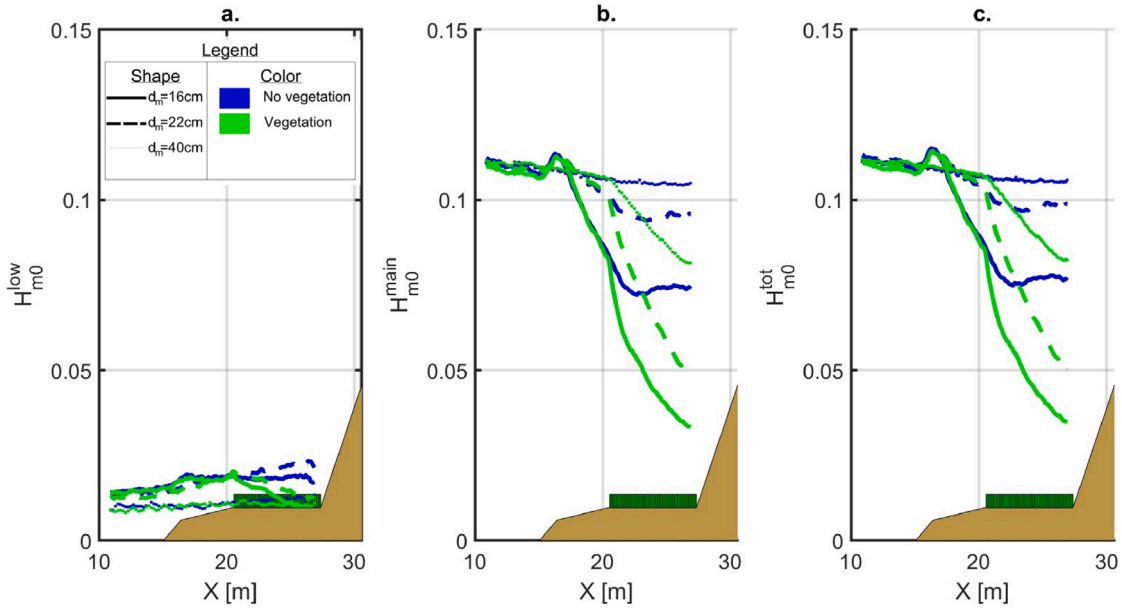

Fig. 7. Evolution of H_{m0} calculated for low (a), main (b) and entire frequency band (c). Three wave conditions (d_m = 0.16, 0.22 and 0.4 m) are compared with h_c = 0 cm, including cases without (*SU1-IR01*, *IR02*, *IR13*) and with vegetation (*SU4-IR01*, *IR02*, *IR013*).

$$\langle e_v \rangle = \frac{\rho C_D D S}{2\sqrt{\pi}} \left(\frac{kg}{2\omega}\right)^3 \frac{sinh^3 kl + 3sinhkl}{3kcosh^3 kd} \left(H^{main}_{rms}\right)^3 \quad (5)$$

where C_D is a bulk drag coefficient. A major assumption in this formula is the validity of linear wave theory to translate the wave height into a velocity field. Moreover, by using a parametrization of $\langle e_v \rangle$ that depends on H^{main}_{rms} only, we implicitly neglect the contribution of the low frequency wave velocity to the total velocity field, and thus to the dissipation induced by the presence of vegetation. This assumption is deemed acceptable as the energy content of the low frequency band compared to the total is small, as was already highlighted in the beginning of this section (Fig. 7).

For the cases without vegetation where $\langle e_v \rangle = 0$, Eq. (3) is solved in the discretized domain from X = 10 m to the toe of the structure (X = 27.35 m) in order to obtain the evolution of E (and thus H^{main}_{rms}) over X (Fig. 8). To better account for the distinct hydrodynamic conditions along the profile, two separate γ_b values are used for each experiment, one over the offshore-foreshore section ($\gamma_{b,f}$, 0–20.47 m) and one over the flat salt marsh platform ($\gamma_{b,m}$, 20.47–27.35, 27.56 or 27.78 m for SU1, SU2 and SU3 respectively). $\gamma_{b,f}$ is determined by finding the value that minimizes the RMSE between the measured incident main wave height at the cliff ($H^{main}_{rms,measured}$, Fig. 8, black line) and the calculated value from Eq. (3) ($H^{main}_{rms,calculated}$, Fig. 8, gray line). Similarly, $\gamma_{b,m}$ is determined as the value that minimizes the RMSE between $H^{main}_{rms,measured}$ and $H^{main}_{rms,calculated}$ over the entire salt marsh platform. Both γ_b values are then used to calculate $\langle e_b \rangle$ (Fig. 8, blue area) for each experiment.

The fitted γ_b values for the foreshore ($\gamma_{b,f}$) and salt marsh platform ($\gamma_{b,m}$) are shown in Fig. 9, taking values mostly between 0.3 and 0.6 across the explored (d_m/L_p) range. The values of $\gamma_{b,f}$ (blue markers) of experiments with more energy dissipation (solid markers, $\int_0^{cliff} \langle e_b \rangle dx > 2.5$ N/s) appear to follow a slightly positive trend with d_m/L_p. On the contrary, in conditions where wave breaking over the foreshore is minimal (transparent markers), $\gamma_{b,f}$ has a negative trend with d_m/L_p, following similar behavior to the results presented in Zhang et al. (2021). $\gamma_{b,m}$ shows a trend akin to $\gamma_{b,f}$, but with larger

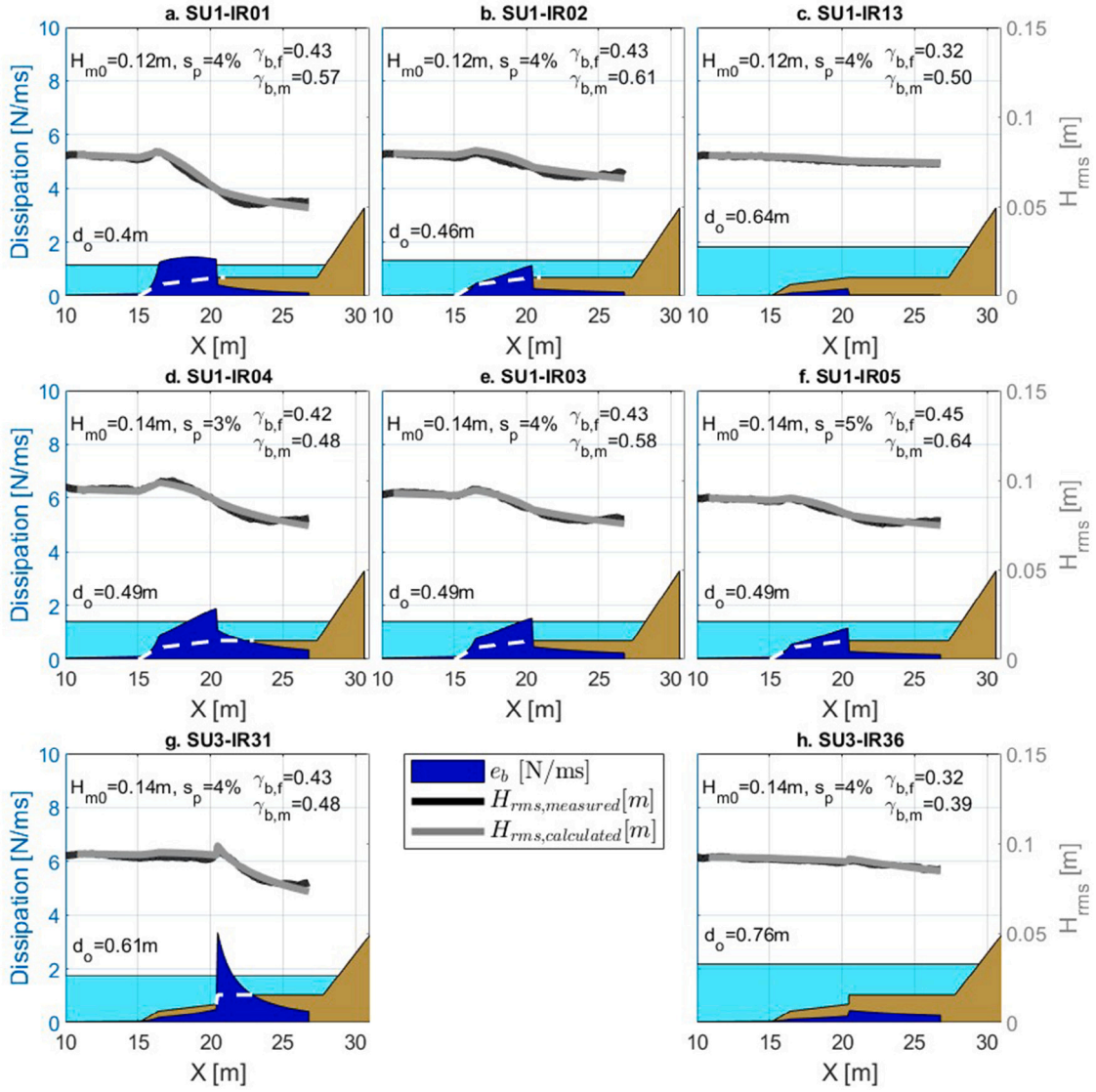

Fig. 8. Example of Eq. (3) application for different offshore water depths (d_o). The black and gray lines show the measured and calculated H_{rms}^{main} (right y-axis) respectively, while the blue area shows the calculated $\langle e_b \rangle$ (left y-axis).

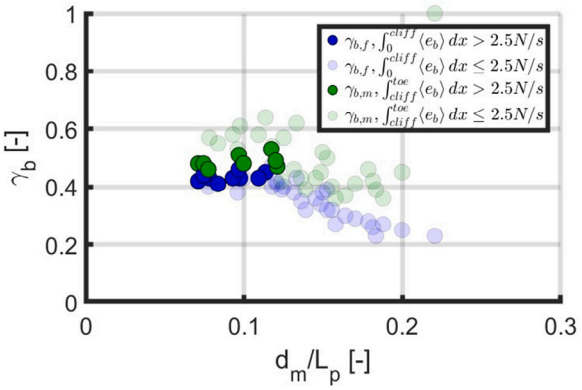

Fig. 9. γ_b values for experiments without vegetation. Blue symbols correspond to $\gamma_{b,f}$ and green symbols to $\gamma_{b,m}$. Marker opacity indicates whether the integrated breaking dissipation in the respective zone exceeds a threshold value of 2.5 N/s.

values to reproduce the smaller wave height decay observed over the horizontal marsh. Despite some local spatial mismatches, the two-zone calibration captures the bulk dissipation over the marsh platform and yields accurate wave-height predictions at the cliff and at the dike toe.

For the vegetated cases, Eq. (3) is applied in each experiment to estimate C_D, maintaining the values of $\gamma_{b,f}$ and $\gamma_{b,m}$ that were determined for the non-vegetated cases. Here, the energy balance incorporates both terms on the right-hand side of Eq. (3), with the spatial domain extending from offshore to the toe of the dike.

In Fig. 10, the results from various vegetation experiments are presented. The top row (Fig. 10a–c) compares identical wave conditions under different offshore water depths. At very shallow water depths (Fig. 10a, $d_o = 0.40$ m), wave energy dissipation is predominantly governed by the foreshore, resulting in minimal energy reaching the vegetated section. As the water depth increases (Fig. 10b, $d_o = 0.49$ m), dissipation by wave breaking is reduced and a larger portion of the incoming energy is transmitted to the vegetated area, leading to a noticeable increase in the total $\langle e_v \rangle$. However, further increasing the depth (Fig. 10c, $d_o = 0.76$ m) reduces the vegetation-induced dissipation, likely due to lower near-bed orbital velocities. The second row (Fig. 10d–f) presents experiments with varying wave steepness. As wave

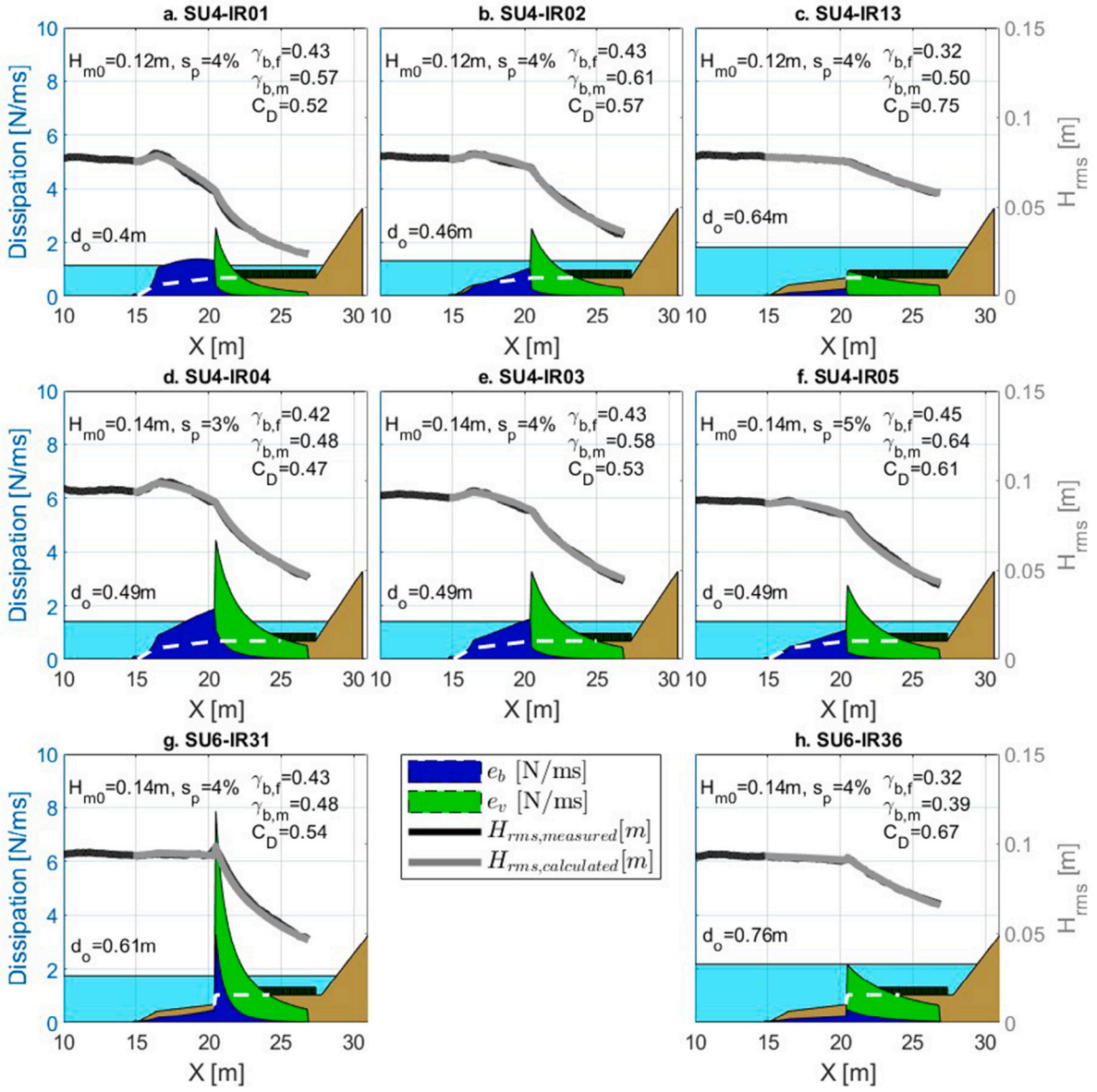

Fig. 10. Example of Eq. (3) application for different d_o. The black and gray lines show the measured ($H_{rms,R}$) and calculated ($H_{rms,ML}$) wave height respectively (right y-axis), the blue and green area show the calculated $\langle e_b \rangle$ and $\langle e_v \rangle$ (left y-axis).

steepness decreases, the total energy dissipation increases, with both $\langle e_b \rangle$ and $\langle e_v \rangle$ becoming more pronounced. The last row (Fig. 10g–h) illustrates the influence of the marsh cliff. Inclusion of a cliff (Fig. 10g) significantly enhances local energy dissipation, while a deeper water level (Fig. 10h) reduces this effect, as the relative water depth difference before and after the cliff becomes less, decreasing shoaling effects.

Fig. 11 summarizes the results of both processes, showing the spatially integrated dissipation induced by breaking $Q_b = \int_{offshore}^{toe} \langle e_b \rangle dx$ and vegetation $Q_v = \int_{cliff}^{toe} \langle e_v \rangle dx$. The value of Q_v is maximum for the cases around $d_m/L_p \approx 0.13$. When $d_m/L_p < 0.1$, intense wave breaking occurs over the foreshore, dissipating significant energy before the waves can interact significantly with the vegetated section. While $d_m/L_p > 0.13$ leads to reduced values of Q_v as a result of reduced orbital velocities at the bottom which leads to less drag and dissipation by vegetation as highlighted above. This indicates the existence of a case-specific threshold depth at which the salt marsh achieves optimal energy dissipation. This threshold is influenced by both the intrinsic properties of the salt marsh and the characteristics of the adjacent foreshore.

Fig. 12 presents a comparison of the measured drag coefficients (C_D) with the empirical formula suggested by Paul and Amos (2011) and Möller et al. (2014). Here, $Re_v = \frac{u_{max} D}{\nu}$ is the Reynolds vegetation number, u_{max} is the 2% highest orbital velocity retrieved from $EMF4$ in the middle of the salt marsh and the color gradient represents the relative water depth d_m/L_p, ranging from 0.06 (dark green) to 0.22 (light green). A clear trend is observed where C_D decreases as Re_v increases, which is consistent with typical drag behavior in wave-vegetation interactions (e.g., Anderson and Smith, 2014; Méndez et al., 1999; Hu et al., 2014). For $Re_v \approx 300$, the calculated drag coefficients align closely with the fitting suggested by Möller et al. (2014). However, as Re_v increases beyond this range, C_D values tend to be higher than the ones measured in previous studies. The color gradient further shows that for very low relative depths (darker green), C_D values are lower as the velocity of non-breaking waves gets lower at the bottom for increasing water depths and decreasing wave lengths (i.e. increasing d_m/L_p). This leads to lower Re_v, a more viscous flow and higher C_D, explaining the observed trend.

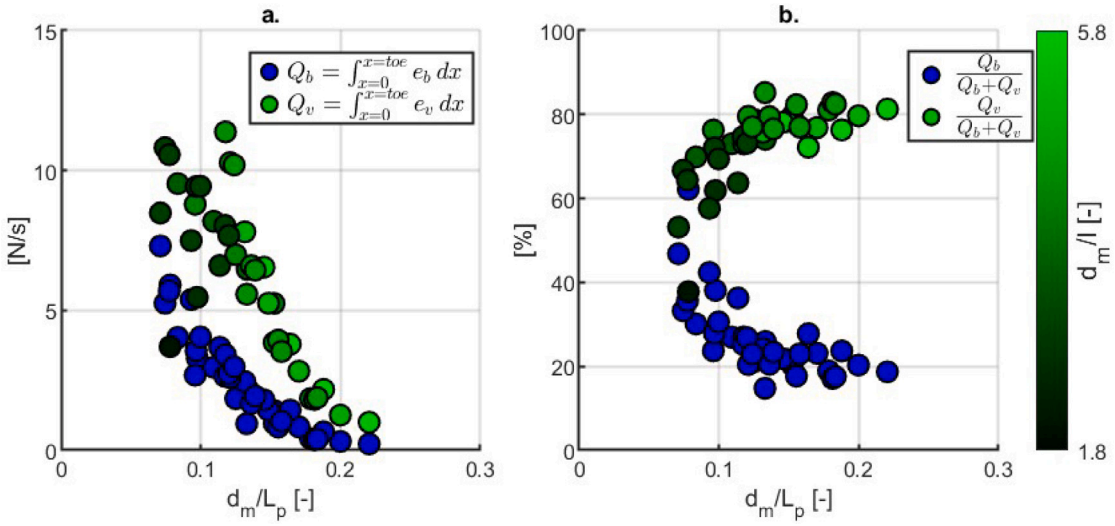

Fig. 11. Energy dissipation over the flume, calculated by spatially integrating e_b and e_v per experiment. Different values of d_m/l are denoted with different hues of green. a: Absolute energy dissipation due to wave breaking and vegetation, b: Dissipation expressed as percentage of the total dissipation.

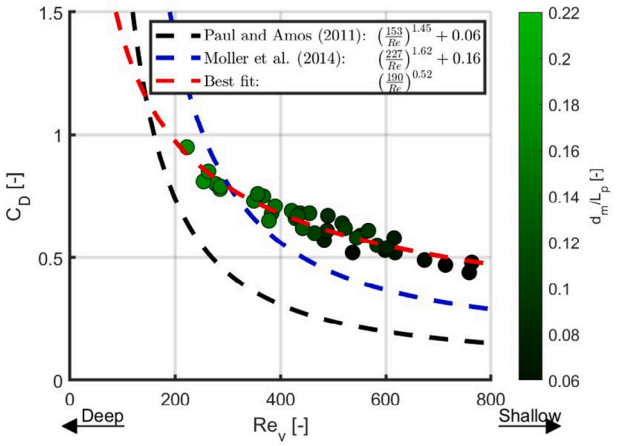

Fig. 12. Comparison of calculated C_D with the fitting by Paul and Amos (2011) and Möller et al. (2014).

3.2. Spectral period

The evolution of $T_{m-1,0}$ is illustrated for three water depths above the salt marsh (d_m = 16, 22, 40 cm) in Fig. 13 calculated for the entire (a) and the main (b) frequency bands. Green lines represent vegetated cases, while blue lines correspond to non-vegetated cases. Considering the non-vegetated scenarios, the spectral period based on the entire frequency range, $T^{tot}_{m-1,0}$ increases with decreasing water depths with a maximum value of 1.18. When vegetation is present, however, the increase of $T^{tot}_{m-1,0}$ is more pronounced, reaching values up to 1.8, with the strongest effects observed at shallower water depths. In studies like Hofland et al. (2017) or Altomare et al. (2016), the value of $T^{tot}_{m-1,0}$ also increases, but the cause is not necessarily the same. For the non-vegetated cases, this increase could be linked to a relatively larger role of the infragravity wave components. For the vegetated cases, however, the infragravity waves might not play a large role in the increase of $T^{tot}_{m-1,0}$, and the cause for the rise in wave period is most probably different.

On the contrary, focusing only the main frequency band, the value of $T^{main}_{m-1,0}$ for the non-vegetated cases remains either constant, or slightly decreases over the foreshore for the two lower water depths i.e. d_m = 0.16–0.22 m) as a result of non-linear energy transfer to higher frequencies (Fig. 5). The vegetation reverses this effect, as after the initial reduction over the foreshore (i.e. between X = 15–20 m), $T^{main}_{m-1,0}$ increases again over the vegetated foreshore reaching values no larger than 1.05 times the offshore one.

To further investigate the specific effect of vegetation on $T_{m-1,0}$, we focus in the following on wave transformation over the second half of the marsh where breaking processes are minimal (see near-zero $\langle e_b \rangle$-values for $X > 23.96$ m in Fig. 10). Fig. 14a shows that when considering the entire frequency range, $T_{m-1,0}$ stays roughly constant for the higher relative water depths considered ($d_m/L_p > 0.13$), with no notable difference between the cases with and without vegetation. For lower relative water depths ($d_m/L_p < 0.13$), there is an increase in $T_{m-1,0}$ for the vegetated cases up to almost 63% over the second half of the marsh, while its value for the non-vegetated cases exhibits smaller increases in the order of 8%. Considering only the main frequency band (Fig. 14b) reveals a similar trend. The values of $T^{main}_{m-1,0}$ for non-vegetated cases reasonably match those of the vegetated cases. $T^{main}_{m-1,0}$ is only slightly larger for the cases of vegetation (up to 10%) when $d_m/L_p < 0.13$. Larger differences appear when comparing $T^{main}_{m-1,0}$ and $T^{tot}_{m-1,0}$ for the cases with vegetation. For both of these cases, the value of $T_{m-1,0}$ does not change for $d_m/L_p < 0.13$, while for $d_m/L_p < 0.13$, $T^{tot}_{m-1,0}$ increases much more compared to $T^{main}_{m-1,0}$.

In an attempt to characterize the shift in spectral shape leading to the observed changes in spectral period, Fig. 15 shows the relative change of spectral energy (m_0) between the middle of the marsh and the toe of the dike for three spectral bands: low ($f/f_p < 0.5$), mid ($0.5 < f/f_p < 1.5$) and high ($f/f_p > 1.5$) frequencies. For the non-vegetated cases, energy above $0.5f_p$ stays relatively constant between the middle of the marsh and the dike toe (blue dots in Fig. 15b,c). The low frequency band (blue dots in Fig. 15a) exhibits a more complex pattern. For the higher relative depths ($d_m/L_p > 0.15$), the energy levels increase mildly by up to 30%, suggesting limited infragravity wave growth. For lower depths, however, $m_{0,toe}/m_{0,middle}$ in the low frequency band increases and reaches a maximum low-frequency growth around 60% obtained for approximately $d/L_p \approx 0.1$. This relative depth corresponds to the minimum depth for which no significant breaking occurs in the most offshore part of the profile (see Fig. 11a). Further decrease of d_m/L_p results in more dissipation by wave breaking and a smaller increase of $m_{0,toe}/m_{0,middle}$. This suggests the existence of an optimum in terms of infragravity wave growth, where the water depth is shallow enough for nonlinearities to be significant and energy transfers to take place, while still being deep enough to prevent significant breaking

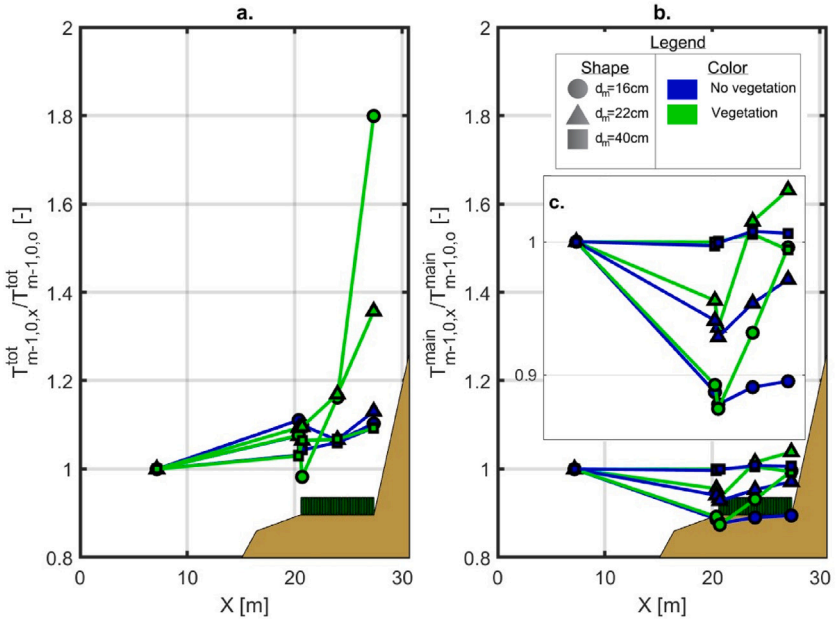

Fig. 13. Spatial evolution of the spectral wave period normalized by its offshore value ($T_{m-1,0,x}/T_{m-1,0,o}$), for experiments with d_m = 12, 22 and 40 cm, with (SU4-IR01, SU4-IR02 and SU4-IR13) and without vegetation (SU1-IR01, SU1-IR02 and SU1-IR13). a: Evolution of $T^{tot}_{m-1,0}$. b: Evolution of $T^{main}_{m-1,0}$. c: Zoom in of subfigure b.

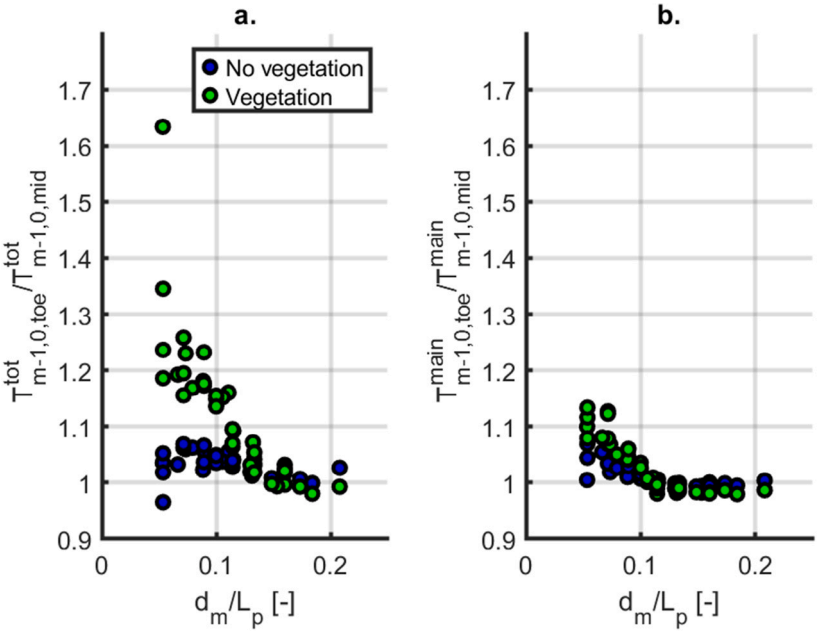

Fig. 14. Evolution of the spectral period $T_{m-1,0}$ from the mid-marsh ($WG4-EMF4$) to the toe of the dike ($WG5-EMF5$), for cases with and without vegetation. a: Evolution of $T^{tot}_{m-1,0}$. b: Evolution of $T^{main}_{m-1,0}$ is calculated only from the main frequency band.

over the outer part of the foreshore, preserving wave groups and thus infragravity wave forcing. This explains the slight increase in spectral period observed around $d_m/L_p \approx 0.1$ for the non-vegetated case in Fig. 14a.

In the presence of vegetation, the energy consistently decreases in all frequency bands ($m_{0,toe}/m_{0,middle} < 1$, see Fig. 15a–c), with an exception in the high-frequency band for large relative depths where the ratio tends to 1 as these short components increasingly behave like deep-water waves and thus exhibit minimal or negligible interaction with the vegetation.

For lower d_m/L_p values (e.g., < 0.1), energy attenuation is more pronounced in the main frequency band than at low frequencies for the cases with vegetation, and becomes even more significant at high frequencies. This highlights the selective nature of vegetation-induced damping, which is considerably more effective for short waves. This frequency-dependent attenuation explains the large increase in $T_{m-1,0}$, which does not indicate an actual increase in low-frequency energy, but rather a shift in the relative distribution of energy across the spectrum; although the total energy is decreasing.

4. Discussion

The results of this study provide insights into the effect a salt marsh has on wave characteristics under varying wave conditions and cliff

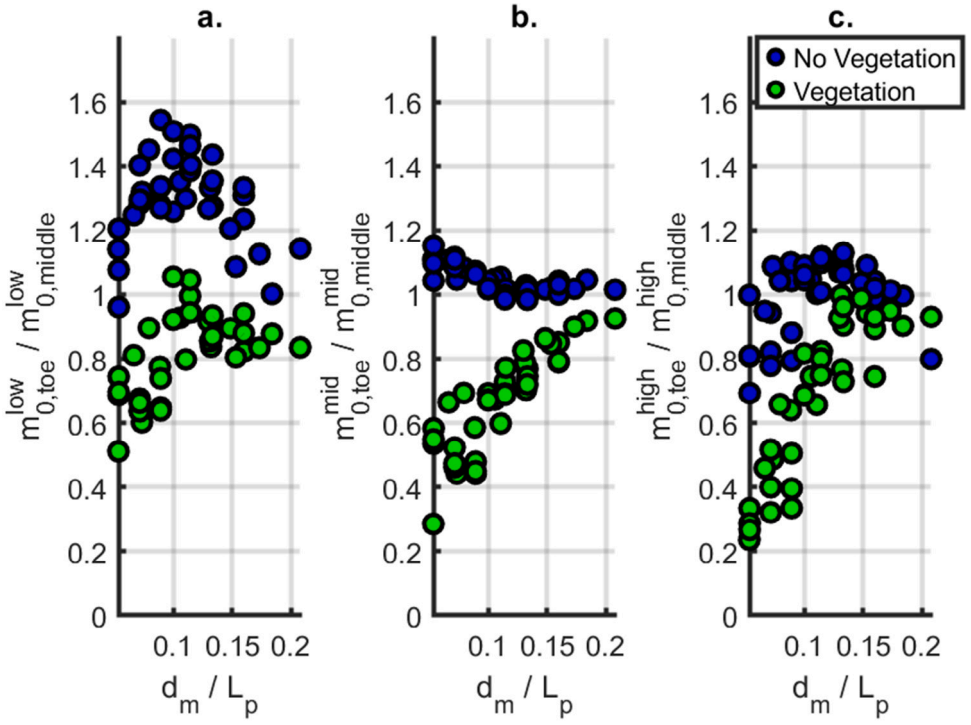

Fig. 15. Ratio between m_0 at the toe ($m_{0,toe}$, $WG5-EMF5$) and at the middle of the salt marsh ($m_{0,mid}$, $WG4-EMF4$), calculated for: a. Low frequency band $f/f_p < 0.5$. b: Mid frequency band ($f/f_p = 0.5-1.5$). c: High frequency band ($f/f_p > 1.5$).

heights. It should be noted that, due to partial reflection at the dike, long waves may form quasi-standing patterns, with nodal structures located within the surf zone. In case a reflection analysis is imperfect, these patterns can particularly influence low-frequency components. Although the applied methods (Almar et al., 2016; Buckley et al., 2015) performed well and the low frequency content in the experiments was low (maximum 5.6% of total energy), this intrinsic wave structure could influence the spatial distribution of infragravity energy observed in the experiments.

The analysis of the wave height shows that the breaking parameter γ_b is not constant. Comparisons between the calculated and observed wave heights at the dike toe in Fig. 8 shows that using more than one γ_b per case leads to a good approximation of the cumulative dissipation by breaking over the profile. Initially, a unique γ_b value was tested for each experiment. However, it resulted in worse match between $H_{rms,measured}$ and $H_{rms,predicted}$ heavily influencing C_D, as through this approach dissipation was underestimated on the sloping part of the foreshore and overestimated it on the horizontal part.

For the vegetated cases, the drag coefficients (C_D) were derived under the assumption of a linear system. In which the energy dissipation components $\langle e_b \rangle$ (due to wave breaking) and $\langle e_v \rangle$ (due to vegetation) are independent while the values of γ_b are assumed to be the same for the cases with and without vegetation. The observed reduction in C_D with increasing Reynolds number (Re_v) aligns with known behaviors in wave-vegetation interactions (e.g., Möller et al., 2014). Despite the merging of multiple plant shoots to increase the vegetations Reynolds number (Re_v), the scaled model still exhibited lower Re_v values than typically observed in natural conditions, which can cause an increase in the observed damping (e.g., Kalloe et al., 2024). The flow around the model vegetation occurs in a more viscous regime for very low Re_v, leading to an increase in C_D and viscous damping, and is expected to be larger than that of a similar model tested at full scale. A single rigid cylinder in flow is expected to have a $C_D \approx 1.2-1.3$ for the range $Re_v \approx 220-780$ (Sumer and Fredsøe, 1997). Applying a kinematic similarity to calculate u on prototype scale and using the vegetation prototype diameter ($D_0 = 8.5$ mm, Table 3) we calculate $Re_v = 2960-10500$ and $C_D \approx 1$. As a result, we can estimate an order of magnitude of 20–30% increased C_D as a result of scaling effects.

This study initially aimed to describe the evolution of $T_{m-1,0}$ along a vegetated salt marsh for dike design purposes. Our analysis revealed that $T_{m-1,0}$ – when defined over the entire frequency band – increased by up to 63% from the middle of the salt marsh to the toe of the dike due to the presence of vegetation. This increase reached a maximum of 8% for the non vegetated cases. Such an increase in spectral period due to vegetation would in turn result in a significant increase in overtopping discharges if this parameter were used as input in commonly-used empirical formulas (e.g. EurOtop, 2018; van Gent, 1999). Interestingly, the observed increase in $T_{m-1,0}$ in the vegetated cases is not due to an actual increase in low-frequency energy, but rather to a relative shift in the spectral distribution, where high-frequency components are more effectively damped than low-frequency ones (e.g., Anderson et al., 2011; Jadhav et al., 2013; Anderson and Smith, 2014; Jacobsen et al., 2019). This selective attenuation alters the spectral shape and is reflected in the variation of $T_{m-1,0}$, but it does not necessarily correspond to more severe hydrodynamic forcing that would justify higher crest elevations or stronger revetments. This suggests that this commonly used spectral parameter may not be appropriate for informing the design of coastal structures or flood defenses located behind a salt marsh. These results highlight the need for a revised or alternative design approach that explicitly accounts for the frequency-dependent damping effect of vegetation, particularly when salt marshes are considered as part of coastal protection strategies.

5. Conclusion

This study highlights the role of salt marshes in coastal protection, particularly through wave energy dissipation, while also examining their impact on wave spectral periods, which have implications for overtopping and coastal vulnerability. By modeling these effects in controlled laboratory conditions, this research highlights how varying wave conditions over varying bottom profiles influence the evolution of the spectral variables reaching the structure behind the salt marsh.

Such findings are valuable as they provide a basis for integrating salt marshes into nature-based solutions that complement traditional hard infrastructure.

The method suggested by Mendez and Losada (2004) is applied to evaluate wave dissipation, observing how wave energy is reduced over the marsh platform and cliff regions. The calculated C_D values showed a good agreement with the fitting suggested by Möller et al. (2014), although higher C_D values were observed for $Re_v > 300$. For very low water depths, the majority of waves are breaking over the barren foreshore, and as a result, the leftover energy dampened by salt marsh vegetation is limited. Increasing water depths lead to an increase in the incoming wave height at the edge of the salt marsh, and the total dissipation done by vegetation increases. Further increase of the water depth leads to a decrease in dissipation, showing that for our specific foreshore-salt marsh set-up, the salt marsh attenuates energy optimally for $d_m/L_p \approx 0.13$.

An analysis of the evolution of the energy in three separate parts of the wave spectrum led to the conclusion that vegetation selectively dampens higher-frequency wave components, leading to an increase in the spectral period $T_{m-1,0}$ across the marsh. However, this increase does not indicate a rise in low-frequency energy, but rather a relative redistribution of spectral energy, where high-frequency components are more strongly attenuated than low-frequency ones. Therefore, $T_{m-1,0}$ may not be a reliable design parameter in vegetated settings, where the frequency-dependent nature of wave damping should be explicitly accounted for.

Further research is required to validate and extend the laboratory findings through field-scale studies incorporating real salt marsh vegetation, particularly in environments with more complex bathymetric profiles. Furthermore, calculations of a spatially varying γ_b should be investigated to improve the precision of wave attenuation estimates. Lastly, further investigation is needed to examine how vegetation-induced increases in $T_{m-1,0}$ influence prediction formulas for wave run-up and overtopping (e.g. EurOtop, 2018), as large increases from the damping of high-frequency components may lead to overestimation.

CRediT authorship contribution statement

Dimitrios Dermentzoglou: Writing – original draft, Methodology, Formal analysis, Data curation, Conceptualization. **Marion Tissier:** Writing – review & editing, Supervision, Formal analysis. **Jos R.M. Muller:** Investigation. **Bas Hofland:** Writing – review & editing. **Stijn Lakerveld:** Writing – review & editing. **Bas W. Borsje:** Writing – review & editing, Conceptualization. **Alessandro Antonini:** Writing – review & editing, Supervision, Formal analysis, Conceptualization.

Declaration of Generative AI and AI-assisted technologies in the writing process

During the preparation of this work the authors used *ChatGPT 4o* in order to enhance the clarity, coherence, and style of the text. After using this tool/service, the authors reviewed and edited the content as needed and take full responsibility for the content of the published article.

Declaration of competing interest

The authors declare that they have no known competing financial interests or personal relationships that could have appeared to influence the work reported in this paper.

Acknowledgments

This work is part of the 'Living Dikes – Realizing resilient and climate-proof coastal protection' project NWA.1292.19.257, funded by the Netherlands Organization for Scientific Research (NWO). Also, we acknowledge the inestimable support of the TU Delft technicians Pieter van der Gaag, Chantal Willems, Arno Doorn, Arie van der Vlies, Frank Kalkman and Jennifer Rietdijk and the help of the University of Twente MSc student Pieter Faber during experiments.

Data availability

Data are available at the 4TU data repository, https://doi.org/10.4121/a2d39670-4a74-4a39-aebd-23956fafacbd.v1.

References

Almar, R., Larnier, S., Castelle, B., Scott, T., Floc'h, F., 2016. On the use of the radon transform to estimate longshore currents from video imagery. Coast. Eng. 114, 301–308. http://dx.doi.org/10.1016/j.coastaleng.2016.04.016, URL: https://www.sciencedirect.com/science/article/pii/S0378383916300643.

Altomare, C., Suzuki, T., Chen, X., Verwaest, T., Kortenhaus, A., 2016. Wave overtopping of sea dikes with very shallow foreshores. Coast. Eng. 116, 236–257. http://dx.doi.org/10.1016/j.coastaleng.2016.07.002, URL: https://www.sciencedirect.com/science/article/pii/S0378383916301260.

Anderson, M., Smith, J., 2014. Wave attenuation by flexible, idealized salt marsh vegetation. Coast. Eng. 83, 82–92. http://dx.doi.org/10.1016/j.coastaleng.2013.10.004, URL: https://www.sciencedirect.com/science/article/pii/S0378383913001609.

Anderson, M.E., Smith, J.M., McKay, S.K., 2011. Wave Dissipation by Vegetation. Technical Report ERDC/CHL CHETN-I-82, U.S. Army Engineer Research and Development Center, Coastal and Hydraulics Laboratory, URL: https://apps.dtic.mil/sti/html/tr/AD1003881/.

Antonini, A., Breteler, M.K., Willemsen, P., Dermentzoglou, D., Muller, J., Mason, V., Bouma, T., Vouziouris, A., Buring, P., Borsje, B., 2024. Large-scale test of extreme hydrodynamic conditions Over Coastal salt marshes. CoastLab 2024 Phys. Model. Coast. Eng. Sci. http://dx.doi.org/10.59490/coastlab.2024.772.

Augustin, L.N., Irish, J.L., Lynett, P., 2009. Laboratory and numerical studies of wave damping by emergent and near-emergent wetland vegetation. Coast. Eng. 56 (3), 332–340. http://dx.doi.org/10.1016/j.coastaleng.2008.09.004, URL: https://www.sciencedirect.com/science/article/pii/S037838390800152X.

Bertin, X., de Bakker, A., van Dongeren, A., Coco, G., André, G., Ardhuin, F., Bonneton, P., Bouchette, F., Castelle, B., Crawford, W.C., Davidson, M., Deen, M., Dodet, G., Guérin, T., Inch, K., Leckler, F., McCall, R., Muller, H., Olabarrieta, M., Roelvink, D., Ruessink, G., Sous, D., Stutzmann, É., Tissier, M., 2018. Infragravity waves: From driving mechanisms to impacts. Earth-Sci. Rev. 177, 774–799. http://dx.doi.org/10.1016/j.earscirev.2018.01.002, URL: https://www.sciencedirect.com/science/article/pii/S0012825217303239.

Best, Ü., Van der Wegen, M., Dijkstra, J., Willemsen, P., Borsje, B., Roelvink, D.J., 2018. Do salt marshes survive sea level rise? Modelling wave action, morphodynamics and vegetation dynamics. Environ. Model. Softw. 109, 152–166. http://dx.doi.org/10.1016/j.envsoft.2018.08.004, URL: https://www.sciencedirect.com/science/article/pii/S1364815217309428.

Bouma, T., Temmerman, S., van Duren, L., Martini, E., Vandenbruwaene, W., Callaghan, D., Balke, T., Biermans, G., Klaassen, P., van Steeg, P., Dekker, F., van de Koppel, J., de Vries, M., Herman, P., 2013. Organism traits determine the strength of scale-dependent bio-geomorphic feedbacks: A flume study on three intertidal plant species. Geomorphology 180–181, 57–65. http://dx.doi.org/10.1016/j.geomorph.2012.09.005, URL: https://www.sciencedirect.com/science/article/pii/S0169555X12004424.

Brooks, H., Möller, I., Carr, S., Chirol, C., Christie, E., Evans, B., Spencer, K.L., Spencer, T., Royse, K., 2021. Resistance of salt marsh substrates to near-instantaneous hydrodynamic forcing. Earth Surf. Process. Landf. 46 (1), 67–88. http://dx.doi.org/10.1002/esp.4912, URL: https://onlinelibrary.wiley.com/doi/abs/10.1002/esp.4912, arXiv:https://onlinelibrary.wiley.com/doi/pdf/10.1002/esp.4912.

Buckley, M.L., Lowe, R.J., Hansen, J.E., Dongeren, A.R.V., 2015. Dynamics of wave setup over a steeply sloping fringing reef. J. Phys. Oceanogr. 45 (12), 3005–3023. http://dx.doi.org/10.1175/JPO-D-15-0067.1, URL: https://journals.ametsoc.org/view/journals/phoc/45/12/jpo-d-15-0067.1.xml.

Callaghan, D., Bouma, T., Klaassen, P., van der Wal, D., Stive, M., Herman, P., 2010. Hydrodynamic forcing on salt-marsh development: Distinguishing the relative importance of waves and tidal flows. Estuar. Coast. Shelf Sci. 89 (1), 73–88. http://dx.doi.org/10.1016/j.ecss.2010.05.013, URL: https://www.sciencedirect.com/science/article/pii/S0272771410002064.

Chen, Q., Zhao, H., 2012. Theoretical models for wave energy dissipation caused by vegetation. J. Eng. Mech. 138 (2), 221–229. http://dx.doi.org/10.1061/(ASCE)EM.1943-7889.0000318, URL: https://ascelibrary.org/doi/abs/10.1061/%28ASCE%29EM.1943-7889.0000318.

Contti Neto, N., Lowe, R.J., Ghisalberti, M., Pomeroy, A., Reidenbach, M., Conde-Frias, M., da Silva, R.F., 2025. Spectral wave energy dissipation by a seagrass meadow. J. Geophys. Res. Ocean. 130 (3), e2024JC020938. http://dx.doi.org/10.1029/2024JC020938, URL: https://agupubs.onlinelibrary.wiley.com/doi/abs/10.1029/2024JC020938.

EurOtop, 2018. Manual on wave overtopping of sea defences and related structures: An overtopping manual largely based on European research, but for worldwide application. Van der Meer, J.W., Allsop, N.W.H., Bruce, T., De Rouck, J., Kortenhaus, A., Pullen, T., Schüttrumpf, H., Troch, P. and Zanuttigh, B.. URL: www.overtopping-manual.com.

Gedan, K.B., Kirwan, M.L., Wolanski, E., Barbier, E.B., Silliman, B.R., 2011. The present and future role of coastal wetland vegetation in protecting shorelines: Answering recent challenges to the paradigm. Clim. Change 106 (1), 7–29. http://dx.doi.org/10.1007/s10584-010-0003-7.

Hofland, B., Chen, X., Altomare, C., Oosterlo, P., 2017. Prediction formula for the spectral wave period Tm-1,0 on mildly sloping shallow foreshores. Coast. Eng. 123, 21–28. http://dx.doi.org/10.1016/j.coastaleng.2017.02.005, URL: https://www.sciencedirect.com/science/article/pii/S037838391630237X.

Hu, Z., Suzuki, T., Zitman, T., Uittewaal, W., Stive, M., 2014. Laboratory study on wave dissipation by vegetation in combined current–wave flow. Coast. Eng. 88, 131–142. http://dx.doi.org/10.1016/j.coastaleng.2014.02.009, URL: https://www.sciencedirect.com/science/article/pii/S0378383914000416.

Jacobsen, N., McFall, B., van der A, D., 2019. A frequency distributed dissipation model for canopies. Coast. Eng. 150, 135–146. http://dx.doi.org/10.1016/j.coastaleng.2019.04.007, URL: https://www.sciencedirect.com/science/article/pii/S0378383918303892.

Jadhav, R.S., Chen, Q., Smith, J.M., 2013. Spectral distribution of wave energy dissipation by salt marsh vegetation. Coast. Eng. 77, 99–107. http://dx.doi.org/10.1016/j.coastaleng.2013.02.013, URL: https://www.sciencedirect.com/science/article/pii/S0378383913000537.

Jalonen, J., Järvelä, J., 2013. Impact of tree scale on drag: Experiments in a towing tank. In: Wang, Z., et al. (Eds.), 35th IAHR World Congress, Chengdu, 8-13 September 2013. Tsinghua University, China, pp. 1–12, VK: 700672; 13133113.

Kalloe, S.A., Hofland, B., Van Wesenbeeck, B.K., 2024. Scaled versus real-scale tests: Identifying scale and model errors in wave damping through woody vegetation. Ecol. Eng. 202, 107241. http://dx.doi.org/10.1016/j.ecoleng.2024.107241, URL: https://www.sciencedirect.com/science/article/pii/S092585742400065X.

Keimer, K., Schürenkamp, D., Miescke, F., Kosmalla, V., Lojek, O., Goseberg, N., 2021. Ecohydraulics of surrogate salt marshes for coastal protection: Wave–Vegetation interaction and related hydrodynamics on vegetated foreshores at sea dikes. J. Waterw. Port Coast. Ocean. Eng. 147 (6), 04021035. http://dx.doi.org/10.1061/(ASCE)WW.1943-5460.0000667, URL: https://ascelibrary.org/doi/abs/10.1061/%28ASCE%29WW.1943-5460.0000667.

Kirwan, M.L., Guntenspergen, G.R., D'Alpaos, A., Morris, J.T., Mudd, S.M., Temmerman, S., 2010. Limits on the adaptability of coastal marshes to rising sea level. Geophys. Res. Lett. 37 (23), http://dx.doi.org/10.1029/2010GL045489, URL: https://agupubs.onlinelibrary.wiley.com/doi/abs/10.1029/2010GL045489.

Kirwan, M.L., Megonigal, J.P., 2013. Tidal wetland stability in the face of human impacts and sea-level rise. Nature 504 (7478), 53–60. http://dx.doi.org/10.1038/nature12856.

Lashley, C.H., van der Meer, J., Bricker, J.D., Altomare, C., Suzuki, T., Hirayama, K., 2021. Formulating wave overtopping at vertical and sloping structures with shallow foreshores using deep-water wave characteristics. J. Waterw. Port Coast. Ocean. Eng. 147 (6), 04021036. http://dx.doi.org/10.1061/(ASCE)WW.1943-5460.0000675, URL: https://ascelibrary.org/doi/abs/10.1061/%28ASCE%29WW.1943-5460.0000675.

Lowe, R.J., Koseff, J.R., Monismith, S.G., 2005. Oscillatory flow through submerged canopies: 1. Velocity structure. J. Geophys. Res. Ocean. 110 (C10), http://dx.doi.org/10.1029/2004JC002788, URL: https://agupubs.onlinelibrary.wiley.com/doi/abs/10.1029/2004JC002788, arXiv:https://agupubs.onlinelibrary.wiley.com/doi/pdf/10.1029/2004JC002788.

Luhar, M., Nepf, H., 2016. Wave-induced dynamics of flexible blades. J. Fluids Struct. 61, 20–41. http://dx.doi.org/10.1016/j.jfluidstructs.2015.11.007, URL: https://www.sciencedirect.com/science/article/pii/S0889974615002613.

Marin-Diaz, B., van der Wal, D., Kaptein, L., Martinez-Garcia, P., Lashley, C.H., de Jong, K., Nieuwenhuis, J.W., Govers, L.L., Olff, H., Bouma, T.J., 2023. Using salt marshes for coastal protection: Effective but hard to get where needed most. J. Appl. Ecol. 60 (7), 1286–1301. http://dx.doi.org/10.1111/1365-2664.14413, URL: https://besjournals.onlinelibrary.wiley.com/doi/abs/10.1111/1365-2664.14413.

Mariotti, G., Fagherazzi, S., 2013. Critical width of tidal flats triggers marsh collapse in the absence of sea-level rise. Proc. Natl. Acad. Sci. 110 (14), 5353–5356. http://dx.doi.org/10.1073/pnas.1219600110, URL: https://www.pnas.org/doi/abs/10.1073/pnas.1219600110.

Maza, M., Lara, J., Losada, I., Ondiviela, B., Trinogga, J., Bouma, T., 2015. Large-scale 3-D experiments of wave and current interaction with real vegetation. Part 2: Experimental analysis. Coast. Eng. 106, 73–86. http://dx.doi.org/10.1016/j.coastaleng.2015.09.010, URL: https://www.sciencedirect.com/science/article/pii/S0378383915001581.

Mcowen, C.J., Weatherdon, L.V., Bochove, J.-W.V., Sullivan, E., Blyth, S., Zockler, C., Stanwell-Smith, D., Kingston, N., Martin, C.S., Spalding, M., Fletcher, S., 2017. A global map of saltmarshes. Biodivers. Data J. 5, e11764. http://dx.doi.org/10.3897/BDJ.5.e11764.

Mendez, F.J., Losada, I.J., 2004. An empirical model to estimate the propagation of random breaking and nonbreaking waves over vegetation fields. Coast. Eng. 51 (2), 103–118. http://dx.doi.org/10.1016/j.coastaleng.2003.11.003, URL: https://www.sciencedirect.com/science/article/pii/S0378383903001182.

Méndez, F.J., Losada, I.J., Losada, M.A., 1999. Hydrodynamics induced by wind waves in a vegetation field. J. Geophys. Res. Ocean. 104 (C8), 18383–18396. http://dx.doi.org/10.1029/1999JC900119, URL: https://agupubs.onlinelibrary.wiley.com/doi/abs/10.1029/1999JC900119, arXiv:https://agupubs.onlinelibrary.wiley.com/doi/pdf/10.1029/1999JC900119.

Miche, M., 1944. Mouvements ondulatoires de la mer en profondeur constante ou décroissante. Ann. Ponts Chaussées 1944, Pp (1) 26-78, (2) 270-292, (3) 369-406.

Möller, I., 2006. Quantifying saltmarsh vegetation and its effect on wave height dissipation: Results from a UK east coast saltmarsh. Estuar. Coast. Shelf Sci. 69 (3), 337–351. http://dx.doi.org/10.1016/j.ecss.2006.05.003, URL: https://www.sciencedirect.com/science/article/pii/S027277140600182X. Salt Marsh Geomorphology: Physical and ecological effects on landform.

Möller, I., Kudella, M., Rupprecht, F., Spencer, T., Paul, M., van Wesenbeeck, B.K., Wolters, G., Jensen, K., Bouma, T.J., Miranda-Lange, M., Schimmels, S., 2014. Wave attenuation over coastal salt marshes under storm surge conditions. Nat. Geosci. 7 (10), 727–731. http://dx.doi.org/10.1038/ngeo2251.

Muller, J., Borsje, B., van der Werf, J., Dermentzoglou, D., Hofland, B., Antonini, A., Hulscher, S., 2026. Wave-driven hydrodynamics around a saltmarsh cliff under storm conditions: the role of cliff height and vegetation. Coast. Eng. 204, 104875. http://dx.doi.org/10.1016/j.coastaleng.2025.104875, URL: https://www.sciencedirect.com/science/article/pii/S0378383925001802.

Myrhaug, D., 2018. Some probabilistic properties of deep water wave steepness. Oceanologia 60 (2), 187–192. http://dx.doi.org/10.1016/j.oceano.2017.10.003, URL: https://www.sciencedirect.com/science/article/pii/S0078323417300970.

Oosterlo, P., Hofland, B., van der Meer, J.W., Overduin, M., Steendam, G.J., 2021. Calibration and preparation of field measurements of oblique wave run-up and overtopping on dikes using laser scanners. Coast. Eng. 167, 103915. http://dx.doi.org/10.1016/j.coastaleng.2021.103915, URL: https://www.sciencedirect.com/science/article/pii/S0378383921000752.

Paul, M., Amos, C.L., 2011. Spatial and seasonal variation in wave attenuation over Zostera noltii. J. Geophys. Res.: Ocean. 116 (C8), http://dx.doi.org/10.1029/2010JC006797, URL: https://agupubs.onlinelibrary.wiley.com/doi/abs/10.1029/2010JC006797, arXiv:https://agupubs.onlinelibrary.wiley.com/doi/pdf/10.1029/2010JC006797.

Pearson, R.K., Neuvo, Y., Astola, J., Gabbouj, M., 2016. Generalized hampel filters. EURASIP J. Adv. Signal Process. 2016 (1), 87. http://dx.doi.org/10.1186/s13634-016-0383-6.

Sumer, B.M., Fredsøe, J., 1997. Hydrodynamics Around Cylindrical Structures. World Scientific, http://dx.doi.org/10.1142/3316, URL: https://www.worldscientific.com/doi/abs/10.1142/3316.

Suzuki, T., Zijlema, M., Burger, B., Meijer, M.C., Narayan, S., 2012. Wave dissipation by vegetation with layer schematization in SWAN. Coast. Eng. 59 (1), 64–71. http://dx.doi.org/10.1016/j.coastaleng.2011.07.006, URL: https://www.sciencedirect.com/science/article/pii/S0378383911001347.

Thornton, E.B., Guza, R.T., 1983. Transformation of wave height distribution. J. Geophys. Res. Ocean. 88 (C10), 5925–5938. http://dx.doi.org/10.1029/JC088iC10p05925, URL: https://agupubs.onlinelibrary.wiley.com/doi/abs/10.1029/JC088iC10p05925.

van der Wal, D., Pye, K., 2004. Patterns, rates and possible causes of saltmarsh erosion in the greater thames area (UK). Geomorphology 61 (3), 373–391. http://dx.doi.org/10.1016/j.geomorph.2004.02.005, URL: https://www.sciencedirect.com/science/article/pii/S0169555X04000674.

van Gent, M.R.A., 1999. Physical Model Investigations on Coastal Structures with Shallow Foreshores: 2D Model Tests with Single and Double-Peaked Wave Energy Spectra. Technical Report, WL|Delft Hydraulics, URL: https://open.rijkswaterstaat.nl/@220768/physical-model-investigations-on-coastal/.

van Gent, M.R.A., 2002. Wave overtopping events at dikes. In: Coastal Engineering 2002. pp. 2203–2215. http://dx.doi.org/10.1142/9789812791306_0185, URL: https://www.worldscientific.com/doi/abs/10.1142/9789812791306_0185.

van Veelen, T.J., Fairchild, T.P., Reeve, D.E., Karunarathna, H., 2020. Experimental study on vegetation flexibility as control parameter for wave damping and velocity structure. Coast. Eng. 157, 103648. http://dx.doi.org/10.1016/j.coastaleng.2020.103648, URL: https://www.sciencedirect.com/science/article/pii/S0378383919300663.

Vuik, V., Jonkman, S.N., Borsje, B.W., Suzuki, T., 2016. Nature-based flood protection: The efficiency of vegetated foreshores for reducing wave loads on coastal dikes. Coast. Eng. 116, 42–56. http://dx.doi.org/10.1016/j.coastaleng.2016.06.001, URL: https://www.sciencedirect.com/science/article/pii/S0378383916301004.

Vuik, V., Suh Heo, H.Y., Zhu, Z., Borsje, B.W., Jonkman, S.N., 2018. Stem breakage of salt marsh vegetation under wave forcing: A field and model study. Estuar. Coast. Shelf Sci. 200, 41–58. http://dx.doi.org/10.1016/j.ecss.2017.09.028, URL: https://www.sciencedirect.com/science/article/pii/S0272771417303918.

Willemsen, P.W., Borsje, B.W., Vuik, V., Bouma, T.J., Hulscher, S.J., 2020. Field-based decadal wave attenuating capacity of combined tidal flats and salt marshes. Coast. Eng. 156, 103628. http://dx.doi.org/10.1016/j.coastaleng.2019.103628, URL: https://www.sciencedirect.com/science/article/pii/S0378383919303345.

Yang, S.L., Shi, B.W., Bouma, T.J., Ysebaert, T., Luo, X.X., 2012. Wave attenuation at a salt marsh margin: A case study of an Exposed Coast on the Yangtze Estuary. Estuaries Coasts 35 (1), 169–182. http://dx.doi.org/10.1007/s12237-011-9424-4.

Zhang, C., Li, Y., Cai, Y., Shi, J., Zheng, J., Cai, F., Qi, H., 2021. Parameterization of nearshore wave breaker index. Coast. Eng. 168, 103914. http://dx.doi.org/10.1016/j.coastaleng.2021.103914, URL: https://www.sciencedirect.com/science/article/pii/S0378383921000740.

Zhang, X., Lin, P., Nepf, H., 2022. A wave damping model for flexible marsh plants with leaves considering linear to weakly nonlinear wave conditions. Coast. Eng. 175, 104124. http://dx.doi.org/10.1016/j.coastaleng.2022.104124, URL: https://www.sciencedirect.com/science/article/pii/S0378383922000412.

Zhang, X., Nepf, H., 2021. Wave-induced reconfiguration of and drag on marsh plants. J. Fluids Struct. 100, 103192. http://dx.doi.org/10.1016/j.jfluidstructs.2020.103192, URL: https://www.sciencedirect.com/science/article/pii/S0889974620306617.

Zhao, K., Liu, P.L.-F., 2022. On Stokes wave solutions. Proc. R. Soc. A: Math. Phys. Eng. Sci. 478 (2258), 20210732. http://dx.doi.org/10.1098/rspa.2021.0732, URL: https://royalsocietypublishing.org/doi/abs/10.1098/rspa.2021.0732.

Zhao, Y., Peng, Z., He, Q., Ma, Y., 2023. Wave attenuation over combined salt marsh vegetation. Ocean Eng. 267, 113234. http://dx.doi.org/10.1016/j.oceaneng.2022.113234, URL: https://www.sciencedirect.com/science/article/pii/S0029801822025173.